

Physical properties and chemical composition of the cores in the California molecular cloud

Guo-Yin Zhang^{1,2,*}, Jin-Long Xu¹, A. I. Vasyunin^{3,4}, D. A. Semenov^{5,6}, Jun-Jie Wang^{1,**}, Sami Dib^{6,7}, Tie Liu^{8,9}, Sheng-Yuan Liu¹⁰, Chuan-Peng Zhang^{1,6}, Xiao-Lan Liu¹, Ke Wang^{11,12}, Di Li^{1,2,13}, Zhong-Zu Wu¹⁴, Jing-Hua Yuan¹, Da-Lei Li¹⁵, and Yang Gao¹⁶

¹ National Astronomical Observatories, Chinese Academy of Sciences, Beijing 100101, China
e-mail: zgyin@nao.cas.cn; e-mail: wangjj@nao.cas.cn

² University of Chinese Academy of Sciences, Beijing 100049, China

³ Ural Federal University, Ekaterinburg, Russia

⁴ Engineering Research Institute ‘Ventspils International Radio Astronomy Centre’ of Ventspils University of Applied Sciences, Inženieru 101, Ventspils LV-3601, Latvia

⁵ Department of Chemistry, Ludwig Maximilian University, Butenandtstr. 5-13, 81377 München, Germany

⁶ Max Planck Institute for Astronomy, Königstuhl 17, D-69117, Heidelberg, Germany

⁷ Niels Bohr International Academy, Niels Bohr Institute, Blegdamsvej 17, DK-2100 Copenhagen Ø, Denmark

⁸ Korea Astronomy and Space Science Institute, 776 Daedeokdaero, Yuseong-gu, Daejeon 34055, Republic of Korea

⁹ East Asian Observatory, 660 N. A’ohoku Place, Hilo, HI 96720, USA

¹⁰ Institute of Astronomy and Astrophysics, Academia Sinica. 11F of Astronomy-Mathematics Building, AS/NTU No.1, Sec. 4, Roosevelt Rd, Taipei 10617, Taiwan

¹¹ Kavli Institute for Astronomy and Astrophysics, Peking University, 5 Yiheyuan Road, Haidian District, Beijing 100871, China

¹² European Southern Observatory (ESO) Headquarters, Karl-Schwarzschild-Str. 2, 85748 Garching bei München, Germany

¹³ CAS Key Laboratory of FAST, NAOC, Chinese Academy of Sciences, Beijing 100101, China

¹⁴ College of Physics, Guizhou University, Guiyang 550025, China

¹⁵ Xinjiang Astronomical Observatory, CAS, 150, Science 1-street, Urumqi, Xinjiang 830011, China

¹⁶ School of Physics and Astronomy, Sun Yat-Sen University, Zhuhai, 519082, Guangdong, China

Received xx xx, xxxx; accepted xx xx, xxxx

ABSTRACT

Aims. We aim to reveal the physical properties and chemical composition of the cores in the California molecular cloud (CMC), so as to better understand the initial conditions of star formation.

Methods. We made a high-resolution column density map (18.2'') with Herschel data, and extracted a complete sample of the cores in the CMC with the *fellwalker* algorithm. We performed new single-pointing observations of molecular lines near 90 GHz with the IRAM 30m telescope along the main filament of the CMC. In addition, we also performed a numerical modeling of chemical evolution for the cores under the physical conditions.

Results. We extracted 300 cores, of which 33 are protostellar and 267 are starless cores. About 51% (137 of 267) of the starless cores are prestellar cores. Three cores have the potential to evolve into high-mass stars. The prestellar core mass function (CMF) can be well fit by a log-normal form. The high-mass end of the prestellar CMF shows a power-law form with an index $\alpha = -0.9 \pm 0.1$ that is shallower than that of the Galactic field stellar mass function. Combining the mass transformation efficiency (ϵ) from the prestellar core to the star of $15 \pm 1\%$ and the core formation efficiency (CFE) of 5.5%, we suggest an overall star formation efficiency of about 1% in the CMC. In the single-pointing observations with the IRAM 30m telescope, we find that 6 cores show blue-skewed profile, while 4 cores show red-skewed profile. The molecular line detection rates of $\text{C}_2\text{H}(1-0)$, HCN , $\text{HCO}^+(1-0)$, and HNC in the protostellar cores are higher than those in the prestellar cores. The detection rates of the $\text{H}^{13}\text{CO}^+(1-0)$, $\text{HN}^{13}\text{C}(1-0)$, and $\text{N}_2\text{H}^+(1-0)$ in the cores are higher than reference positions that are offset from the cores. $[\text{HCO}^+]/[\text{HNC}]$ and $[\text{HCO}^+]/[\text{N}_2\text{H}^+]$ in protostellar cores are higher than those in prestellar cores; this can be used as chemical clocks. The best-fit chemical age of the cores with line observations is $\sim 5 \times 10^4$ years.

Key words. ISM – giant molecular cloud – astrochemistry – astrophysics

1. Introduction

The California molecular cloud (CMC) is atypical among the local giant molecular clouds (GMCs) (Lada et al. 2009, 2017). The CMC is in an early state of evolution and has not achieved the internal physical conditions to promote more active star formation,

so it is significantly deficient in its star formation activity compared to other well-known clouds of its size and mass, such as Orion A and B, Rosette, NGC 2264, and W3 (Kutner et al. 1977; Williams et al. 1995; Dahm 2008; Rivera-Ingraham et al. 2013). The CMC shows a filamentary structure with a distance of 450 ± 23 pc and mass of $\sim 10^5 M_\odot$ (Lada et al. 2009). The hottest part of the CMC is located in its southeast, and it might be illuminated by a B star LkHα101 (Barsony et al. 1991). Although

* Just to show the usage of the elements in the author field

** Just to show the usage of the elements in the author field

many investigations have been performed in the past decade by Lada et al. (2009); Harvey et al. (2013); Li et al. (2014); Kong et al. (2015); Lada et al. (2017); Broekhoven-Fiene et al. (2018), the physical properties and chemical composition of the dense cores in the CMC are still not well understood.

The dense cores in molecular clouds are birthplaces of stars (Alves et al. 2007; Lada et al. 2008; André et al. 2014; Hony et al. 2015). There is intense debate in the literature on whether the core mass function (CMF) and the initial mass function (IMF) of the newly formed stars possess the same underlying mass distribution. A few studies have suggested that this might be the case in a number of low-mass star-forming regions (e.g., Alves et al. 2007; Könyves et al. 2010). For the Pipe nebula cloud, Alves et al. (2007) argued that the CMF of the cloud is similar to the IMF of the Trapezium cluster (Muench et al. 2002), with an offset that is suggestive of a core-to-star efficiency, ϵ , of ≈ 0.3 . Recent CMF determinations challenge this picture. Motte et al. (2018) showed that the CMF of dense cores in the W43 massive star-forming region is much shallower than the Galactic field IMF. Furthermore, a number of recent studies have pointed to significant cluster-to-cluster variations in the parameters that characterize the shape of the IMF in young Galactic and extra-galactic clusters (Dib 2014; Weisz et al. 2015; Dib et al. 2017; Schneider et al. 2018). From a theoretical perspective, several works have discussed the time-dependent nature of the CMF and how its shape can be affected by ongoing accretion onto prestellar cores (e.g., Dib et al. 2010) and in closely packed systems by core coalescence (Shadmehri 2004; Dib et al. 2007a).

Molecular abundance ratios can be used to estimate the evolutionary stages of the dense cores; these are known as chemical clocks. Various pairs of molecules have been proposed over time to serve as chemical clocks that can be used to evaluate the evolutionary stages of the dense cores, including pairs of cyanopolyyynes (Stahler 1984) or oxygen-bearing to nitrogen-bearing species (e.g., Doty et al. 2002). Although it was debated whether abundances of chemical species can be used as direct estimates of the physical age of protostellar clouds (see, e.g., Gerin et al. 2003), the chemical age can still be used to estimate the evolutionary status of the objects of interest, and it can be compared with well-studied regions of star formation. For example, the young chemical age of the core can be an indication of its young physical age, if the abundances of chemical species are similar to those in a well-studied object that was proven to be young by other studies. The CMC is significantly deficient in its star formation activity, which makes it a good example on which to confirm whether ϵ is truly a constant, or if it varies with the environment. Furthermore, when a core is chemically young, the question arises whether a set of molecules can trace its evolution. In order to address these questions, we need to examine the CMC in more detail.

It is therefore important to understand why the California GMC shows less prominent star formation activity than other more active GMCs. To do this, we have to constrain its gas and dust properties, such as density, temperature, kinematics, and chemical composition. We therefore identified cores in a Herschel dust continuum map, and we employed the IRAM 30m antenna to observe the bright lines of CO, N₂H⁺, HCN, HNC, HCO⁺, and CCH and the CO, HNC, and HCO⁺ isotopologues in the individual cores and other star-forming environments. This combination of molecular tracers allows us to probe gas temperature and density (CO, N₂H⁺, and HCN/HNC), ionization (HCO⁺ and N₂H⁺), and the local high-energy radiation intensity (C₂H/HCN). The paper is organized as follows: In Sect. 2 we describe the observations and data reduction. We present and

discuss the results in Sects. 3 and 4, respectively. A summary is provided in Sect. 5.

2. Observations and data reduction

2.1. Herschel archival data

The Herschel data include PACS 70 and 160 μm (Poglitsch et al. 2010) and SPIRE 250, 350, and 500 μm (Griffin et al. 2010) imaging for the CMC (Harvey et al. 2013)¹. We used the Harvey et al. (2013) version instead of the current HSA pipeline products, see Harvey et al. (2013), to determine the details in observations and data reduction processes. We focused on a region of the CMC that covers about 18 square degrees. An image at the Herschel 500 μm band for this region is shown in Fig. 1. The parallel-mode observations with a fast scan speed 60'' s^{-1} were made with two PACS bands and three SPIRE bands. The beam sizes of the PACS at 70 μm and 160 μm are 8.4'' and 13.5'', respectively. The beam sizes of the SPIRE at 250 μm , 350 μm , and 500 μm are 18.2'', 24.9'', and 36.3'', respectively.

2.2. Molecular line observations

2.2.1. Source selection

To explore the chemical properties of the cold dense cores in the CMC, we selected 30 positions for single-pointing observations with the IRAM 30m telescope. The observed positions are located along the main filament of the CMC. Of these 30 positions, 18 are associated with the CSO Bolocam 1.1mm sources (Harvey et al. 2013). In order to obtain an unbiased sample with different physical conditions, we also selected another 12 high column density positions based on the Herschel column density map (Harvey et al. 2013). These positions are shown in Fig. 2 and Table 1.

2.2.2. Single-pointing observations with the IRAM 30m

Single-pointing observations near 90 GHz were carried out in April 2014 using the IRAM 30m telescope on Pico Veleta, Spain. The frequency coverage includes the molecular transitions H¹³CO⁺(1 – 0), HN¹³C(1 – 0), C₂H(1 – 0), HCN(1 – 0), HCO⁺(1 – 0), HNC(1 – 0), N₂H⁺(1 – 0), C¹⁸O(1 – 0), and ¹³CO(1 – 0). The single-pixel heterodyne receiver of the Eight MIXer Receiver (EMIR) with a bandwidth of 16 GHz in two orthogonal polarizations was employed to simultaneously observe these nine lines. The fast Fourier transform spectrometer (FTS) backends were set to 200 kHz (about 0.65 km s^{-1} at 90 GHz) resolution. We averaged the two orthogonal polarizations. We fit linear baselines and subtracted them from the data. The molecular lines were converted from the antenna temperature (T_A^*) into the main-beam temperature (T_{mb}) scale by multiplying with the ratio of forward efficiency to main-beam efficiency ². The forward efficiency from 86 GHz to 115 GHz is from 81% to 78%. The main-beam efficiency from 86 GHz to 115 GHz is from 95% to 94%. The beam sizes are 29'' at 86 GHz and 23'' at 110 GHz, corresponding to the spatial resolutions of 0.063 pc and 0.05 pc, respectively, at the distance of the CMC (450 pc). The typical rms level is 0.05 K for H¹³CO⁺(1 – 0), HN¹³C(1 – 0), C₂H(1 – 0), HCN(1 – 0), HCO⁺(1 – 0), HNC(1 – 0), N₂H⁺(1 – 0), and 0.09 K

¹ <http://irsa.ipac.caltech.edu/data/Herschel/ACMC/>

² <http://www.iram.es/IRAMES/mainWiki/Iram30mEfficiencies>

for C¹⁸O(1 – 0) and ¹³CO(1 – 0). All spectra data were reduced with the GILDAS³ software package.

3. Results

3.1. Herschel H₂ column density results

3.1.1. Herschel high-resolution H₂ column density map

We applied the *getsources* tool to derive the column density map of the CMC. *Getsources* (Men'shchikov et al. 2010, 2012; Men'shchikov 2013) is a multi-scale, multi-wavelength source extraction algorithm. The bash script *hirescoldens* in *getsources* was used to create the high-resolution H₂ column density maps (18.2'') with Herschel four-band emission from 160 to 500 μm. The *Hirescoldens* methods are described in Appendix A of Palmeirim et al. (2013). The zero-level offsets in the Herschel images are estimated from the Planck and IRAS space telescope (Bernard et al. 2010). In simple words, this method uses a thin graybody model to fit the spectral energy distributions (SEDs) on a pixel-by-pixel basis,

$$I_\nu = B_\nu(T_d)\kappa_\nu\Sigma, \quad (1)$$

where I_ν is the surface brightness at frequency ν , T_d is dust temperature at each map pixel, $B_\nu(T_d)$ is the Planck black-body function, and we assumed a dust opacity law $\kappa_\nu = 0.1 \times (\nu/1000 \text{ GHz})^\beta \text{ cm}^2 \text{ g}^{-1}$ with $\beta = 2$ (Hildebrand 1983; Palmeirim et al. 2013), and Σ is the surface density distribution.

3.1.2. Core extraction from the H₂ column density map

We took two steps to extract dense cores from the column density map. First, in order to let the cores stand out, we removed the large-scale diffuse structure in the molecular cloud with *cupid feedback* (Berry et al. 2007). The noise level is $5 \times 10^{20} \text{ cm}^{-2}$, which was determined from off-sources regions in the H₂ column density map. We set the smoothing scale to 95'' judged by visual inspection. Second, we extracted cores from the column density map using the *fellwalker* algorithm developed by Berry (2015). This algorithm considers all pixels with a value above the noise level. It identifies cores by following the steepest gradient route from each pixel in the map until a significant peak is reached. Each such peak is associated with a single core, and all pixels along routes that end at the same peak are assigned to the associated core. Thus cores extracted by *fellwalker* are irregular in shape. However, *fellwalker* can produce an elliptical approximation to the core shape, centered on the peak value in the core. It does this by first searching for the azimuthal angle that gives the largest marginal profile. With this marginal profile as the major axis, the minor axis is then assumed to be perpendicular to the major axis. The length of each marginal profile is the weighted mean of the distances from the peak to each pixel along the profile, weighted by the pixel data values. A scaling factor is then applied that results in the marginal profile length being equal to the FWHM of the equivalent Gaussian. In other words, for a truly Gaussian core, the final major and minor axes of the elliptical fit would be equal to the FWHM of the Gaussian. Finally, we identified 300 cores in the CMC, which are shown in Fig. 3. The detailed *fellwalker* setup is listed in Table 2.

3.1.3. Physical parameters in the identified cores

The mass of the core is given by the integral of the column density across the core:

$$M = \mu_{\text{H}_2} m_{\text{H}} \int \Sigma_{\text{H}_2} dA, \quad (2)$$

where $\mu_{\text{H}_2} = 2.8$ is the molecular weight per hydrogen molecule. m_{H} is the H atom mass. A is the area of the core.

L_{maj} is the major axis of the ellipse, L_{min} is the minor axis. They are equal to the FWHMs of the equivalent Gaussian core. The effective deconvolved radii of the cores were calculated as

$$R_{\text{eff}} = \frac{\sqrt{(L_{\text{maj}}^2 - \text{FWHM}_{250\mu\text{m}}^2)} \times \sqrt{(L_{\text{min}}^2 - \text{FWHM}_{250\mu\text{m}}^2)}}{2} \quad (3)$$

The volume (V) of the core is $(4/3)\pi R^3$ on the assumption that it is spherical. Then the number density of hydrogen molecule $n(\text{H}_2)$ in the core is $M/(\mu_{\text{H}_2} * m_{\text{H}})/V$. The derived masses of the cores are in the range of $0.1 \sim 32.9 \text{ M}_\odot$, with an average value of 1.9 M_\odot . The radii of the cores are in the range of $0.01 \sim 0.1 \text{ pc}$, with an average value of 0.04 pc . The number densities are in the range of $1 \times 10^4 \sim 1.5 \times 10^6 \text{ cm}^{-3}$, with an average value of $1 \times 10^5 \text{ cm}^{-3}$. The dust temperatures and the H₂ number densities are estimated by averaging the values within the fitting ellipse shape. The dust temperatures of the cores are in the range of $12 \sim 34 \text{ K}$, with an average value of 15 K . The core parameters are summarized in Table 3.

3.1.4. Classification of the dense cores

Based on the presence or absence of young stellar objects (YSOs) detected in the infrared data, Enoch et al. (2009) and Dunham et al. (2016) classified the cores into protostellar or starless cores. Harvey et al. (2013) and Broekhoven-Fiene et al. (2014) have indentified two YSO catalogs in the CMC, respectively. In order to resolve the disagreement between these two studies, Lada et al. (2017) reexamined the YSO classifications with the method employed in Lewis & Lada (2016). The YSO distribution in the CMC is shown in Fig. 4. According to the classification and the new YSO catalog in Lada et al. (2017), we found 33 protostellar cores, accounting for 11% of the total cores. In addition, the prestellar cores are the self-gravitating starless cores. The critical Bonnor-Ebert (BE) mass can be used to substitute the virial mass (Ebert 1955; Bonnor 1956; Könyves et al. 2010). The critical BE mass can be calculated as

$$M_{\text{crit}}^{\text{BE}} \approx \frac{2.4R_{\text{BE}}k_B T}{G\mu_p m_{\text{H}}}, \quad (4)$$

where R_{BE} is the BE radius, determined by the effective radii of the cores, μ_p is the mean molecular weight per free particle. Assuming an abundance ratio $N(\text{H})/N(\text{He}) = 10$, $\mu_p = 2.33$ (Kauffmann et al. 2008). Following Könyves et al. (2010), the assumption of ambient cloud temperature ($T=10 \text{ K}$) is adopted. G is the gravitational constant. k_B is the Boltzmann constant. We identified 137 prestellar cores, accounting for about 51% of the starless cores.

3.1.5. Core mass function and core formation efficiency

Salpeter (1955) initially proposed a power-law IMF:

$$\frac{dN_\star}{d\log M_\star} \propto M_\star^{-\alpha}, 0.4 \text{ M}_\odot < M_\star < 10 \text{ M}_\odot, \quad (5)$$

³ <http://www.iram.fr/IRAMFR/GILDAS/>

where dN_\star is the number of stars in the mass range $d\log M_\star$ and $\alpha = 1.35$. Chabrier (2003) postulated a log-normal IMF to replace the spliced power laws,

$$\frac{dN_\star}{d\log M_\star} \propto \exp\left[-\frac{(\log M_\star - \log \mu)^2}{2\sigma^2}\right], M_\star \leq 1 M_\odot, \\ \propto M_\star^{-1.35}, M_\star \geq 1 M_\odot, \quad (6)$$

where $\mu = 0.08$ and $\sigma = 0.67$. These parameters changed to $\mu = 0.25$ and $\sigma = 0.55$ in Chabrier (2005). μ denotes the peak value of the log-normal form IMF in units of M_\odot and σ is the variance in units of $\log(M_\odot)$.

The core mass function is the mass distribution of the dense cores. In Table 3, the mass of the identified prestellar cores ranges between 0.3 and $13 M_\odot$. We fit the prestellar CMF with power-law and log-normal forms. Here, we did not take into account the errors in mass estimates, but only statistical uncertainties: \sqrt{N} . The fitting results are shown in Fig. 5. The prestellar cores heavier than $1 M_\odot$ can be well fit with a power-law function with $\alpha = -0.9 \pm 0.1$, which is shallower than the power-law index of Salpeter (1955). The log-normal fitting result is $\mu = 1.7 \pm 0.1$ and $\sigma = 0.37 \pm 0.03$. By comparing this with the peak value of the stellar mass of $0.25 M_\odot$ obtained from the Chabrier (2005) IMF, we suggest that the mass transformation efficiency ϵ in the CMC from the prestellar core to the star is about $15 \pm 1\%$.

In addition, the core formation efficiency (CFE) is the ratio of the total core mass to cloud mass,

$$CFE = \frac{M_{\text{core}}}{M_{\text{cloud}}}. \quad (7)$$

We checked the column density map and selected the region without sources to estimate the noise level σ . σ is about $5 \times 10^{20} \text{ cm}^{-2}$. The cloud effective mass is $1.1 \times 10^4 M_\odot$, which was derived by accounting for emission above the 3σ (see Fig. 4). The total core mass is $600 M_\odot$. Therefore the CFE is 5.5%.

3.2. Molecular-line observations

3.2.1. 30 single pointings

The molecular transitions near 90 GHz have typical critical densities ($\gtrsim 10^5 \text{ cm}^{-3}$) for collisional excitation, which makes them excellent tracers for probing dense and cold cores (Foster et al. 2011). Based on the IRAM 30m telescope, 30 positions were observed along the main filament in the CMC. The properties of molecular lines at the 30 positions are summarized in Table 4. We found that 14 positions are protostellar cores, 7 positions are prestellar cores, 8 positions are reference positions that are offset from cores, and 1 position is projected on galaxy 3C111.

Fig. 6 shows $\text{H}^{13}\text{CO}^+(1-0)$, $\text{HN}^{13}\text{C}(1-0)$, $\text{C}_2\text{H}(1-0)$, $\text{HCN}(1-0)$, $\text{HCO}^+(1-0)$, $\text{HNC}(1-0)$, $\text{N}_2\text{H}^+(1-0)$, $\text{C}^{18}\text{O}(1-0)$, and $^{13}\text{CO}(1-0)$ spectra. We detected $^{13}\text{CO}(1-0)$ at all the observed positions, but $\text{C}^{18}\text{O}(1-0)$ only at 27 positions. Generally, the $\text{C}^{18}\text{O}(1-0)$ emission is optically thin, therefore we used $\text{C}^{18}\text{O}(1-0)$ to determine the local standard of rest velocity (V_{LSR}). For the remaining three position without $\text{C}^{18}\text{O}(1-0)$ detections, we used $^{13}\text{CO}(1-0)$ to determine the V_{LSR} . The V_{LSR} ranges from -3.63 to 0.52 km s^{-1} . The systemic velocities, line widths, peak intensities, and velocity-integrated intensities were obtained by fitting Gaussian profiles. The obtained parameters of molecular lines at the 30 observed positions are given in Table 4. The detection rates of each molecular line in the 14 protostellar cores, 7 prestellar cores, and the other reference positions are shown in Fig. 7. We also give the detection rates of each molecular line in Table 5. The detection rates of $\text{C}_2\text{H}(1-0)$, HCN ,

$\text{HCO}^+(1-0)$, and HNC in protostellar cores are higher than that in prestellar cores. Other molecular lines are roughly the same. We also found that the detection rates of the $\text{H}^{13}\text{CO}^+(1-0)$, $\text{HN}^{13}\text{C}(1-0)$, and $\text{N}_2\text{H}^+(1-0)$ in protostellar and prestellar cores are higher than that in the reference positions.

3.2.2. Column density and abundance

We used the ratio with the main isotopologue to determine the optical depths for isotopologue pairs H^{13}CO^+ and HCO^+ , and HN^{13}C and HNC . Assuming that the line excitation is at local thermodynamical equilibrium (LTE), the radiative transfer equation that involves the measured brightness temperature (T_r) is given by

$$T_r = [J(T_{\text{ex}}) - J(T_{\text{bg}})] \times [1 - \exp(-\tau)] f. \quad (8)$$

T_{mb} is the corrected main-beam temperature. We have $T_r = T_{\text{mb}}$. f is the beam filling factor. $J_v(T) = \frac{\frac{h\nu}{k}}{\exp(\frac{h\nu}{k_B T}) - 1}$. T_{bg} is the background temperature of the Universe (2.7 K), while T_{ex} is the excitation temperature of the molecular line. τ is the optical depth. For the molecular isotopologue pair, H^{13}CO^+ and HCO^+ , we assumed that the former is optically thin, but the latter is optically thick. We also assumed that they have the same excitation temperature and beam filling factor.

The optical depths of H^{13}CO^+ and HCO^+ were obtained by comparing the measured brightness temperatures:

$$\frac{T_r(\text{HCO}^+)}{T_r(\text{H}^{13}\text{CO}^+)} \approx \frac{1 - \exp(-\tau_{12})}{1 - \exp(-\tau_{13})}. \quad (9)$$

Furthermore,

$$\frac{\tau_{12}}{\tau_{13}} = \frac{[^{12}\text{C}]}{[^{13}\text{C}]}. \quad (10)$$

The isotopic abundance ratio of $[^{12}\text{C}/^{13}\text{C}]$ is in the range of 20 – 70 (Savage et al. 2002). This value is about 20 in the Galactic center, 53 ± 4 in the 4 kpc molecular ring, and 69 ± 6 in the local interstellar medium (ISM) (Wilson 1999). This value in our solar system is 89 (Lang 1980). Following Sanhueza et al. (2012), we assumed a constant abundance ratio of 50 for $[\text{HCO}^+/\text{H}^{13}\text{CO}^+]$ in the CMC. We obtained the optical depths of HN^{13}C and HNC with the same approach.

$\text{HCN}(1-0)$, $\text{N}_2\text{H}^+(1-0)$ and $\text{C}_2\text{H}(1-0)$ have a hyperfine structure. We calculated the optical depths of these molecular lines with the HyperFine Structure (HFS) method in the CLASS software. The nuclear spin of the nitrogen nucleus leads to the $\text{HCN}(1-0)$ rotational transitions showing three components (Loughnane et al. 2012). The optical depth for its main component $\text{JF} = (12 - 01)$ was calculated. $\text{N}_2\text{H}^+(1-0)$ shows seven components (Keto & Rybicki 2010). Because closely spaced components overlapped, we observed three clusters of lines for $\text{N}_2\text{H}^+(1-0)$. Two of three lines have three components. Only $\text{JF}_1\text{F} = (101 - 012)$ is separated from other components, through which we estimated the optical depth of this component. $\text{C}_2\text{H}(1-0)$ shows six hyperfine components (Padovani et al. 2009). We estimate the optical depth of the main component as $\text{JF} = (3/2, 2 - 1/2, 1)$.

Under the assumption of LTE, the column densities at 30 observation positions were estimated via (Mangum & Shirley

2015)

$$N_{\text{tot}} = \left(\frac{3h}{8\pi^3 S \mu^2 R_i} \right) \left(\frac{Q_{\text{rot}}}{g_J g_K g_I} \right) \frac{\exp\left(\frac{E_u}{k_B T_{\text{ex}}}\right)}{\exp\left(\frac{h\nu}{k_B T_{\text{ex}}}\right) - 1} \times \frac{1}{f(J_\nu(T_{\text{ex}}) - J_\nu(T_{\text{bg}}))} \frac{\tau_\nu}{1 - \exp(-\tau_\nu)} \int T_{\text{mb}} dv, \quad (11)$$

where h is the Planck constant. S is the line strength. μ is the permanent dipole moment along the axis of symmetry of the molecule⁴. R_i is the relative intensity normalized to 1. Q_{rot} is the rotational partition function. E_u is the upper energy. g_J is the rotational degeneracy, g_K is the K degeneracy, and g_I is the nuclear spin degeneracy. We assume that $f = 1$. For the $J \rightarrow = 1 - 0$ transition of linear molecules:

$$\begin{aligned} S &= \frac{J_u}{2J_u + 1} = \frac{1}{3} \\ Q_{\text{rot}} &\approx \frac{\kappa T}{hB_0} + \frac{1}{3} \\ g_J &= 2J_u + 1 = 3 \\ g_K &= 1 \\ g_I &= 1 \end{aligned}, \quad (12)$$

where J_u is the upper energy level quantum number. For $J = 1 - 0$, $J_u = 1$. B_0 is the rigid rotor rotation constant. At high densities of cores ($> 10^5 \text{ cm}^{-3}$), the gas-dust will start to closely couple via collisions (see, e.g., Goldsmith & Langer 1978; Burke & Hollenbach 1983; Goldsmith 2001; Bergin & Tafalla 2007), so we adopted T_{ex} as T_d .

In contrast, for non-LTE-based calculations of $N(X)$, multiple transitions of a species X are required, which we do not have. We have observed the CO isotopologues HCO^+ , HNC, HCN, C_2H , and N_2H^+ in their ground rotational (1-0) transition. We examined the validity of the LTE assumption and applied this assumption to the column density calculation. Usually, in cold sources this occurs when the gas density is higher than the so-called critical density by a factor of 10 or more (Pavlyuchenkov et al. 2008). The critical density is the gas density that is required to start to populate the upper energy level and to excite the line. These densities have been computed for various molecules in a number of papers, see, for example, Shirley (2015). While for the CO (1-0) line the critical density is $\sim 10^3 \text{ cm}^{-3}$, at low T of $\sim 10 \text{ K}$. In contrast, the critical densities are higher for $\text{HCO}^+(1 - 0)$, $\text{HCN}(1 - 0)$, $\text{HNC}(1 - 0)$ and $\text{N}_2\text{H}^+(1 - 0)$, $> \sim 10^5 \text{ cm}^{-3}$. This implies that at $\sim 10 \text{ K}$, these (1-0) lines could be subthermally excited, and our column density estimates are underestimated by a factor of several.

Under the optically thin assumption, the column densities of ^{13}CO and C^{18}O are calculated. The average optical depths are shown in Fig. 8. The calculation parameters are listed in Table 6. The molecular abundances can be defined as $N_{\text{tot}}/N(\text{H})$, where $N(\text{H}) = 2 \times N(\text{H}_2)$. The statistics of molecular abundances toward 14 protostellar cores and 7 prestellar cores are given in Table 7.

3.2.3. Virial masses

We estimated virial mass from the formula below (MacLaren et al. 1988; Bertoldi & McKee 1992),

$$M_{\text{vir}} = \frac{kR\sigma^2}{G}, \quad (13)$$

where k depends on the core density distribution. Following Parikka et al. (2015), we adopted $k = 1.333$, which corresponds to a sphere with a power-law density profile $\rho \propto r^{-1.5}$. Here, $\text{C}^{18}\text{O}(1 - 0)$ was used to calculate the virial mass. The velocity dispersion σ is given by

$$\sigma = \sqrt{\frac{k_B T_{\text{kin}}}{\mu m_{\text{H}}} + \left(\frac{\Delta V_{\text{obs}}^2}{8\ln 2} - \frac{k_B T_{\text{kin}}}{\mu_{\text{tracer}} m_{\text{H}}} \right)}, \quad (14)$$

where T_{kin} is the kinetic temperature. We adopted the dust temperature of core as its kinetic temperature. μ_{tracer} is the mass of the observed molecule. ΔV_{obs} is the observed line width. The observed line width consists of thermal and nonthermal components. $\frac{kT_{\text{kin}}}{\mu_{\text{tracer}} m_{\text{H}}}$ is the thermal component of the observed molecular line, while $\frac{\Delta V_{\text{obs}}^2}{8\ln 2} - \frac{kT_{\text{kin}}}{\mu_{\text{tracer}} m_{\text{H}}}$ is the nonthermal component. The $\text{C}^{18}\text{O}(1 - 0)$ virial masses of our cores are in the range of $1.4 - 5.4 \text{ M}_{\odot}$, with an average value of 3.2 M_{\odot} , which is lower than the average mass of the corresponding cores obtained from the Herschel column density map.

The virial parameter can be given by $\alpha_{\text{vir}} = M_{\text{vir}}/M$, where M is the mass of the core. When we neglect the contributions of the magnetic field and surface terms in the virial equation, it is considered that cores are gravitationally bound whenever $\alpha_{\text{vir}} < 1$ (e.g., Bertoldi & McKee 1992; Dib et al. 2007b). The virial parameter α_{vir} versus the masses of the cores are displayed in Fig. 9. For two prestellar cores, we found that the values of α_{vir} are close to unity, which may indicate that these cores are in a state of near equipartition between gravity and thermal+turbulent support. For the $\text{C}^{18}\text{O}(1 - 0)$ line, 10 out of 12 of the protostellar cores are gravitationally bound according to their α_{vir} values, and 7 prestellar cores display a similar behavior. This is in agreement with the analysis based on estimates of their BE masses.

3.2.4. Chemical age

We performed a numerical modeling of chemical evolution under the physical conditions typical for a core in the early phase of its evolution. We constructed a model of a "typical core" using the information on the physical condition from Table 3. These are the physical conditions for a "typical core": a gas density of $1 \times 10^5 \text{ cm}^{-3}$, $T_{\text{gas}} = T_{\text{dust}} = 15 \text{ K}$, and a visual extinction $\text{Av} = 10$. The cosmic ray ionization rate and the elemental abundances in the CMC are unclear, therefore we took a typical value of $1.3 \times 10^{-17} \text{ s}^{-1}$ for the ionization rate, and the typical "low metal" abundances (EA1 in Wakelam & Herbst (2008)) were used as the initial chemical composition. We used a 0D numerical gas-grain chemical model, that is, a model without any assumptions about the spatial distribution of the species (Vasyunin et al. 2009; Vasyunin & Herbst 2013; Vasyunin et al. 2017). This chemical model is based on (Vasyunin et al. 2017). It employs rate-equation-based three-phase treatment of gas-grain chemistry (gas-ice surface - icy bulk) and the chemical network initially published in Semenov et al. (2010) and then further modified in Vasyunin & Herbst (2013) and Vasyunin et al. (2017). In contrast to Vasyunin et al. (2017), who used a 1D model that consisted of 128 0D models and allowed us to calculate 1D distributions of molecules versus radius in the well-studied core L1544, we here calculated just one representative 0D point, because we currently lack knowledge of the inner structure of the cores in CMC to basically calculate the chemical evolution of a unit volume of gas-dust mixture under the provided physical conditions. The chemical age is the evolutionary time when the

⁴ <http://www.cv.nrao.edu/php/splat/>

modeled abundances of the species match the observed values best. We used the modeling results to estimate the chemical age of observed cores. The best-fit criterion is described in Vasyunin et al. (2017) (Eq. 17). The modeling results are shown in Fig. 10. There, we show the fractional abundances of species versus time. The best agreement between the model and observations is attained at $\sim 5 \times 10^4$ years.

4. Discussion

4.1. Star formation scenario

From the Herschel high-resolution H₂ column density map, we identified 300 cores in the CMC. According to Kauffmann et al. (2010), if the mass of the core is greater than $580M_{\odot}(R/\text{pc})^{1.33}$, where R is the effective radius of the core, then they have the potential of forming massive stars. Fig. 11 presents a mass versus radius plot of the identified cores in the CMC. We found that three cores, CMCHerschel-121, CMCHerschel-276, and CMCHerschel-290, lie above the threshold, indicating that they are dense and massive enough to potentially form massive stars. The mass of CMCHerschel-121 is about $33 M_{\odot}$, while its effective radius is about 0.08 pc. In our IRAM 30m observations, it is called CMC-9. From Fig. 6, we found that there is a self-absorption dip in the optically thick line HNC(1 – 0) of this core, and a blue-skewed profile for HCN(1 – 0) and HCO⁺(1 – 0). We therefore suggest that this core is a collapsing high-mass core candidate. The mass of CMCHerschel-276 is about $4.9 M_{\odot}$; we did not observe it with the IRAM 30m telescope. CMCHerschel-290 is called CMC-29 in our IRAM 30m observations. The mass is about $12 M_{\odot}$ and the radius is about 0.03 pc. There are no blue or red profiles in its molecular lines. It is relatively quiet.

Fig. 12 shows part of the filament that contains the high-mass core (CMCHerschel-121). The local noise level σ is $1.3 \times 10^{21} \text{ cm}^{-2}$ in the Herschel H₂ column density map. We estimate the filament mass to be above 3σ . The mass of this filament is about $291.9 M_{\odot}$, while the length is 6.6 pc. The linear mass is about $44.2 M_{\odot} \text{ pc}^{-1}$. The critical linear mass density for the turbulent pressure to dominate the thermal pressure can be estimated by $(M/l)_{\text{max}} = 84(\Delta V)^2 M_{\odot} \text{ pc}^{-1}$ (Jackson et al. 2010). Our IRAM 30m observations include three positions in this filament: CMC-7, CMC-8, and CMC-9. The average C¹⁸O(1 – 0) FWHM is 0.84 km s^{-1} . The critical line mass from the C¹⁸O(1 – 0) width is $59.3 M_{\odot} \text{ pc}^{-1}$, suggesting that the turbulent pressure can support the filament against gravitational collapse.

Turbulence plays an important role in star formation processes (Klessen 2001; Ballesteros-Paredes et al. 2007; Dib et al. 2007b; Liu et al. 2012; Federrath & Klessen 2012; Padoan et al. 2017). The CMF fit from numerical models of turbulent fragmentation in the molecular clouds is more similar to a log-normal form than a power-law form (e.g., Dib & Burkert 2005; Ballesteros-Paredes et al. 2006; Dib et al. 2008; Bailey & Basu 2013; Gong & Ostriker 2015, but see also Padoan & Nordlund 2011; Hennebelle 2018). We find that the CMF of prestellar cores in the CMC is well fit by a log-normal distribution, suggesting that turbulence takes an important role in shaping the CMF.

Based on the offset between the CMF of the Pipe nebula cloud and the IMF of the Trapezium, Alves et al. (2007) proposed that the core-to-star efficiency, ϵ is about $30\% \pm 10\%$. However, they did not take into account that some of the cores in their sample may not be prestellar in nature. Because of the low resolution of the Bolocam 1.1 mm, Enoch et al. (2008) only give

a lower limit on ϵ 25% for Perseus, Serpens, and Ophiuchus. The prestellar ϵ is about 40% in Aquila (André et al. 2010; Könyves et al. 2015). Nutter & Ward-Thompson (2007) found a turnover at $1.3 M_{\odot}$ for SCUBA 850 μm starless cores in Orion. Compared with the turnover at $0.1 M_{\odot}$ for a Kroupa (2002) IMF, the starless ϵ in Orion is about 8%. Compared with the turnover at $0.25 M_{\odot}$ for a Chabrier (2005) IMF, the starless ϵ in Orion is about 19%. The prestellar ϵ of about $15 \pm 1\%$ in the CMC is lower than that in other molecular clouds. The turnover mass of the prestellar CMF in the CMC is $\sim 1.7 M_{\odot}$. This value is close to the critical BE mass ($1.82 M_{\odot}$) for a density of 10^4 cm^{-3} and a gas temperature of 10 K (Lada et al. 2008). It is also close to that ($\sim 2 - 3 M_{\odot}$), which is an indication that thermal fragmentation may be responsible for the CMF in the Pipe nebula (Lada et al. 2008). We note that like the CMC, the Pipe nebula is a cloud with relatively low star formation for its mass and size.

The CFE is about 5.5% in the CMC, which matches the values of 4.9% and 5.5% in the interarm and spiral-arm regions of the Galactic plane from $l = 37^{\circ}83$ to $42^{\circ}50$ with $|b| \leq 0.5^{\circ}$ (Eden et al. 2013). The CFEs for the large-scale structures in our Galaxy are markedly similar in range, but this value is greatly affected by the local environment. The CFE for W3 GMC is 5%-13% in the diffuse region, while it is 26%-37% in the compressed region as a result of the expansion of W 4 H II region. The feedback from the H II regions also leads to a higher CFE and thus enhanced star formation efficiency (Liu et al. 2015, 2017; Xu et al. 2018). The star formation efficiency (SFE) is the fraction of cloud mass that is converted into stars. Combining the ϵ and CFE in the CMC, we suggest that the SFE is about 1 % in the CMC. The typical value in the Milky Way is about 2% (Evans 1991).

The best-fit chemical age of $\sim 5 \times 10^4$ years is well consistent with the hypothesis the CMC is in an early state of evolution, which is somewhat younger than the chemical age for the prototypical prestellar core L1544 (1.6×10^5 years, see, e.g., Jiménez-Serra et al. (2016); Vasyunin et al. (2017)), but there is a difference of one order of magnitude with L134N and TMC-1 (6×10^5 years, Charnley et al. (2001)), and the value is a factor of ~ 20 lower than the estimated lifetime of the prestellar cores in Aquila (1.2×10^6 years) (Könyves et al. 2015). Obviously, determining the chemical age with a single-point 0D model is merely a rough estimation, as is the concept of the "chemical age" itself. The zero-point in terms of the physical conditions that enter the determination of the chemical age is usually ill defined, and thus, a chemical age is prone to being affected by uncertainty. In addition to this, uncertainties in astrochemical models also limit the accuracy of modeled abundances of species to a factor of a few at best for simple species (Vasyunin et al. 2004, 2008; Wakelam et al. 2005, 2006, 2010). As such, a precise estimation of the chemical age is not physically meaningful. Nevertheless, an order-of-magnitude estimation of this value can be a useful tool to confirm the evolutionary status of protostellar objects (Stahler 1984; Williams 1993; Doty et al. 2002; Brünken et al. 2014).

It is also interesting to estimate how stable the best-fit chemical age is to variations in the model parameters, since our definition of a "typical core" as an average of the core parameters from Table 3 may be considered as somewhat too vague and general. We ran a set of models in which the temperatures of gas and dust were varied by ± 5 K and the gas density was varied by a factor of 2. We found that variations of gas and dust temperature in the range [10 – 20] K shift the best-fit chemical age in the range [$4.0 - 5.5 \times 10^4$ years, while variations in gas density by a factor of 2 vary the chemical age in the range [$3.0 - 7.3 \times 10^4$ years. We can therefore conclude that the chemical age is not a pre-

cise value, since it depends on uncertain parameters. However, an order-of-magnitude estimation of the chemical age is useful because this value in the CMC, which is lower than that in well-studied cores in other clouds, implies that the cores in the CMC are indeed young and the CMC is in a very early evolutionary stage.

4.2. Dynamics

The line widths extracted from single-point observation hold important information on the core kinematics. The average widths of $^{13}\text{CO}(1-0)$ and $\text{C}^{18}\text{O}(1-0)$ are 1.6 and 0.92 km s $^{-1}$ in the CMC, which roughly corresponds to those in the Planck cold dust clumps (1.3 km s $^{-1}$ for ^{13}CO and 0.8 km s $^{-1}$ for C^{18}O) (Wu et al. 2012) and those with valid detections of HCO^+ or HCN (1.67 km s $^{-1}$ for ^{13}CO and 1.08 km s $^{-1}$ for C^{18}O) in Yuan et al. (2016). We calculated the asymmetry parameter (Mardones et al. 1997), $\delta V = (V_{\text{thick}} - V_{\text{thin}})/dV_{\text{thin}}$. The asymmetry parameter has been used to quantify the asymmetry of an optical thick molecular line, where V_{thick} is the peak velocity of an optical thick line. V_{thin} is the peak velocity of an optical thin line. dV_{thin} is the full width at half-maximum of the optically thin line. A line is considered to have a blue-skewed profile if $\delta V < -0.25$, and it is red-skewed if $\delta V > 0.25$. The optically thick line $\text{HCO}^+(1-0)$ is a good tracer of the motion of infall. Usually, $\text{HCO}^+(1-0)$ and $\text{HNC}(1-0)$ are optically thick, and $\text{C}^{18}\text{O}(1-0)$ is optically thin. Evidence of infall motion is observable in self-absorbed and optically thick line profiles, which show a combination of a double peak with a brighter blue peak or a skewed single blue peak, or optically thin lines that peak at the self-absorption dip of the optically thick line (He et al. 2015). We find that six cores show a blue-skewed profile and four cores show a red-skewed profile that possibly indicates outflowing motions. The skewed profiles of the molecular line are shown in Table 8.

4.3. Chemical composition

HCN and HCO^+ have high permanent dipole moments. They are good tracers of high-density gas ($\geq 10^6 \text{ cm}^{-3}$), therefore, their emissions are well suited to studying the densest regions in a molecular cloud. The line widths of $\text{HCN}(1-0)$ and $\text{HCO}^+(1-0)$ at the observed positions are in the range of 0.66 ~ 2.65 km s $^{-1}$ and 0.66 ~ 2.81 km s $^{-1}$, with an average value of 1.41 km s $^{-1}$ and 1.49 km s $^{-1}$, respectively. The velocity-integrated intensities of HCN and HCO^+ are in the range of 0.28 ~ 4.63 and 0.29 ~ 8.25 K km s $^{-1}$, with an average value of 1.66 and 3.04 K km s $^{-1}$, respectively. We found strong linear correlations between $\text{HCN}(1-0)$ and $\text{HCO}^+(1-0)$ in line widths and velocity-integrated intensities. The line widths are $W_{\text{HCO}^+} = 0.94 \times W_{\text{HCN}}$ and $R_{\text{Adj}}^2 = 0.73$. R_{Adj}^2 is the adjusted R-squared, that is, the fit residuals relative to the error (variance) estimates, which is an important parameter to indicate how well some terms fit a curve or line. $R_{\text{Adj}}^2 = 0.73$ indicates that about 85% of the data points can be well represented by the fitted line. The velocity-integrated intensities are $I_{\text{HCO}^+} = 1.61 \times I_{\text{HCN}}$ and $R^2 = 0.77$. $R^2 = 0.77$ indicates that about 88% of the data points can be well represented by the fitted line. We show these strong linear relationships between HCN and HCO^+ in Fig. 13. The intensities of HCN and HCO^+ in infrared dark clouds show a linear relation, $I_{\text{HCO}^+} = 1.32 \times I_{\text{HCN}}$ (Liu et al. 2013). Yuan et al. (2016) found that the intensities of HCN and HCO^+ in Planck cold clumps could be fit by a power-law relation, $I_{\text{HCO}^+} = 2.3 \times I_{\text{HCN}}^{0.8}$.

The tight correlation between the line widths and line intensities of HCN and HCO^+ in various CMC cores is due to the two-body nature of the chemical processes by which these species are formed and destroyed, and the lack of strong line excitation gradients in a typical molecular cloud core (Turner 1995; Turner et al. 1997). The denser the core, the more readily both of these molecules form through ion-molecule and neutral-neutral gas-phase reactions. Similarly, the denser the core, the more efficiently HCO^+ dissociates in collisions with electrons, while HCN freezes out more efficiently onto dust grains.

The HCN synthesis is driven by a slow neutral-neutral reaction $\text{N} + \text{CH}_2 \rightarrow \text{HCN} + \text{H}$, and later, a chemical quasi steady-state is attained. This equilibrium is governed by a protonation-recombination cycle: $\text{HCN} + \text{H}_3^+ \rightarrow \text{HCNH}^+ + \text{H}_2$, $\text{HCNH}^+ + \text{e}^- \rightarrow \text{HCN} + \text{H}$, with a 34% probability⁵. The HCO^+ chemistry begins with the conversion of almost the entire C budget into CO, which can then react with H_3^+ to form HCO^+ and H. Later, a chemical steady-state is attained for HCO^+ , with the protonation of CO followed by the dissociative recombination of HCO^+ back into H and CO. The direct chemical relationship between HCO^+ and HCN through common or closely related reactions is quite limited. Only one chemical reaction in our chemical model may lead to the direct correlation between HCO^+ and HCN: $\text{HCO}^+ + \text{HCN} \rightarrow \text{HCNH}^+ + \text{CO}$. However, at least in the model considered, this reaction is a destruction channel of moderate importance (up to 15% of total HCN destruction rate at 10^5 years, and up to 7% of total HCO^+ destruction rate at 10^4 years of evolution).

The abundances of the isomer pair HNC and HCN are roughly equal at low temperature (Irvine & Schloerb 1984; Schilke et al. 1992; Ungerechts et al. 1997; Graninger et al. 2014). The average observed abundances of HNC and HCN are roughly equal in the CMC. The value of $\sim 10^{-9}$ for the HNC and HCN abundance also match previous works well (Hirota et al. 1998; Padovani et al. 2011). We found that the average abundance ratio of HCN/HNC in protostellar cores does not have a clear difference with that in prestellar cores.

A combination of the CO optically thin isotopologue and N_2H^+ , for example, can be employed to estimate the degree of the CO freeze-out, which can also be used as a coarse indicator of the core age and the onset of the star formation process. The main reaction that effectively removes N_2H^+ from the gas when CO is still present is $\text{N}_2\text{H}^+ + \text{CO} \rightarrow \text{HCO}^+ + \text{N}_2$. Later, after $\sim 10^5 - 10^6$ years, when substantial CO freeze-out is expected to occur in dense cores, this destruction channel becomes inefficient. The average abundance ratio of $\text{HCO}^+/\text{N}_2\text{H}^+$ in protostellar cores is about three times higher than that in prestellar cores. We also found that the average abundance ratio of HCO^+/HNC in protostellar cores is about twice higher than that in prestellar cores. There are obvious differences for HCO^+/HNC and $\text{HCO}^+/\text{N}_2\text{H}^+$ in the protostellar cores with the prestellar cores. We therefore suggest that HCO^+/HNC and $\text{HCO}^+/\text{N}_2\text{H}^+$ are chemical clocks. Our results are similar to those of previous studies (e.g., Sanhueza et al. 2012; Hoq et al. 2013).

5. Conclusions

We made a high-resolution (18.2'') H_2 column density map with the Herschel data. Using this map, we extracted a complete core sample with the *fellwalker* algorithm. In order to estimate the chemical composition and evolution of the cores in the CMC,

⁵ http://kida.obs.u-bordeaux1.fr/reaction/2815/HCNH+_+e-.html?filter=Both

we used the IRAM 30m telescope to carry out new single-point molecular line observations near 90 GHz along the CMC main filament. These molecular lines include ^{13}CO (1–0), C^{18}O (1–0), N_2H^+ (1–0), HNC (1–0), HCO^+ (1–0), HCN (1–0), C_2H (1–0), HN^{13}C (1–0), and H^{13}CO^+ (1–0). The main results are summarized as follows:

- (1) We extracted 300 cores from the high-resolution H_2 column density map. These identified cores contain 33 protostellar cores, 137 prestellar cores, and 130 unbound starless cores. The number of the prestellar cores accounts for about 51% of the starless cores.
- (2) The core masses are in the range of $0.12 \sim 33 \text{ M}_\odot$ with an average value of 1.9 M_\odot , while the radii are in the range of $0.01 \sim 0.1 \text{ pc}$ with an average value of 0.04 pc . Three cores can evolve into high-mass stars. The mass of the high-mass core CMC Herschel-121 is 33 M_\odot , while its radius is 0.08 pc . Moreover, this core, located at a filament, shows an infall feature, suggesting that this core may be in a state of collapse.
- (3) The prestellar core CMF is slightly steeper than the Galactic field IMF. The prestellar core CMF can be fit by a lognormal distribution with a peak value $\mu = 1.7 \text{ M}_\odot$ and $\sigma = 0.37 \pm 0.03$. When fit by a power law in the high-mass end, the exponent of the power law is -0.9 ± 0.1 . It should be noted, however, that the CMC is very young, and thus, its population of dense cores is likely to still have ongoing accretion, which will tend to modify or flatten the CMF (Dib et al. 2010). Based on the position of the peak of the CMF with respect to the value of the peak in the (Chabrier 2005) IMF, we propose that the core-to-star efficiency, ϵ , at this stage of its evolution is $15 \pm 1\%$. With a CFE of $\approx 5.5\%$, this translates into an SFE of $\approx 1\%$.
- (4) Based on the IRAM 30m telescope single-pointing observations at 30 positions, we find that six cores show a blue-skewed profile and four cores show a red-skewed profile.
- (5) The detection rates of H^{13}CO^+ (1–0), HN^{13}C (1–0), and N_2H^+ (1–0) in the protostellar or prestellar cores are clearly higher than the reference positions. Additionally, the detection rates of the molecular lines of C_2H (1–0), HCN , HCO^+ (1–0), and HNC in protostellar cores are higher than those in the prestellar cores.
- (6) The line widths and line intensities of HCN correlate well with those of HCO^+ . $[\text{HCO}^+]/[\text{HNC}]$ and $[\text{HCO}^+]/[\text{N}_2\text{H}^+]$ in protostellar cores are obviously higher than those in prestellar cores, which can be used as chemical clocks.
- (7) The best-fit chemical age of the cold cores is about 5×10^4 years, which we derived by fitting the data with an elaborate chemical model.

Acknowledgements. We acknowledge valuable comments from the referee. We thank Charles J. Lada for useful discussion on the manuscript. We thank A. Men'shchikov, D. S. Berry, and S. Bardeau for their technical support with Getsources, Starlink and Gildas, respectively. This work is supported by National Key R&D Program of China (No. 2017YFA0402600; 2017YFA0402702), National Key Basic Research Program of China (973 Program) (No. 2015CB857101), National Natural Science foundation of China (No. 11703040; 11703074; 11721303; 11763002; U1431111), and Chinese Government Scholarship (No. 201804910583). D.A.S. acknowledges support from the Heidelberg Institute of Theoretical Studies for the project ?Chemical kinetics models and visualization tools: Bridging biology and astronomy?. A.I.V. acknowledges support by the Russian Science Foundation (No. 18-12-00351). K.W. acknowledges support by the German Research Foundation (grant WA3628-1/1).

- André, P., Di Francesco, J., Ward-Thompson, D., et al. 2014, Protostars and Planets VI, 27
- André, P., Men'shchikov, A., Bontemps, S., et al. 2010, A&A, 518, L102
- Bailey, N. D. & Basu, S. 2013, ApJ, 766, 27
- Ballesteros-Paredes, J., Gazol, A., Kim, J., et al. 2006, ApJ, 637, 384
- Ballesteros-Paredes, J., Klessen, R. S., Mac Low, M.-M., & Vazquez-Semadeni, E. 2007, Protostars and Planets V, 63
- Barsony, M., Schombert, J. M., & Kis-Halas, K. 1991, ApJ, 379, 221
- Bergin, E. A. & Tafalla, M. 2007, ARA&A, 45, 339
- Bernard, J.-P., Paradis, D., Marshall, D. J., et al. 2010, A&A, 518, L88
- Berry, D. S. 2015, Astronomy and Computing, 10, 22
- Berry, D. S., Reinhold, K., Jenness, T., & Economou, F. 2007, in Astronomical Society of the Pacific Conference Series, Vol. 376, Astronomical Data Analysis Software and Systems XVI, ed. R. A. Shaw, F. Hill, & D. J. Bell, 425
- Bertoldi, F. & McKee, C. F. 1992, ApJ, 395, 140
- Bonnor, W. B. 1956, MNRAS, 116, 351
- Broekhoven-Fiene, H., Matthews, B. C., Harvey, P., et al. 2018, ApJ, 852, 73
- Broekhoven-Fiene, H., Matthews, B. C., Harvey, P. M., et al. 2014, ApJ, 786, 37
- Brünken, S., Sipilä, O., Chambers, E. T., et al. 2014, Nature, 516, 219
- Burke, J. R. & Hollenbach, D. J. 1983, ApJ, 265, 223
- Chabrier, G. 2003, ApJ, 586, L133
- Chabrier, G. 2005, in Astrophysics and Space Science Library, Vol. 327, The Initial Mass Function 50 Years Later, ed. E. Corbelli, F. Palla, & H. Zinnecker, 41
- Charnley, S. B., Rodgers, S. D., & Ehrenfreund, P. 2001, A&A, 378, 1024
- Dahm, S. E. 2008, The Young Cluster and Star Forming Region NGC 2264, ed. B. Reipurth, 966
- Dib, S. 2014, MNRAS, 444, 1957
- Dib, S., Brandenburg, A., Kim, J., Gopinathan, M., & André, P. 2008, ApJ, 678, L105
- Dib, S. & Burkert, A. 2005, ApJ, 630, 238
- Dib, S., Kim, J., & Shadmehri, M. 2007a, MNRAS, 381, L40
- Dib, S., Kim, J., Vázquez-Semadeni, E., Burkert, A., & Shadmehri, M. 2007b, ApJ, 661, 262
- Dib, S., Schmeja, S., & Hony, S. 2017, MNRAS, 464, 1738
- Dib, S., Shadmehri, M., Padoan, P., et al. 2010, MNRAS, 405, 401
- Doty, S. D., van Dishoeck, E. F., van der Tak, F. F. S., & Boonman, A. M. S. 2002, A&A, 389, 446
- Dunham, M. M., Offner, S. S. R., Pineda, J. E., et al. 2016, ApJ, 823, 160
- Ebert, R. 1955, ZAP, 37, 217
- Eden, D. J., Moore, T. J. T., Morgan, L. K., Thompson, M. A., & Urquhart, J. S. 2013, MNRAS, 431, 1587
- Enoch, M. L., Evans, II, N. J., Sargent, A. I., & Glenn, J. 2009, ApJ, 692, 973
- Enoch, M. L., Evans, II, N. J., Sargent, A. I., et al. 2008, ApJ, 684, 1240
- Evans, II, N. J. 1991, in Astronomical Society of the Pacific Conference Series, Vol. 20, Frontiers of Stellar Evolution, ed. D. L. Lambert, 45–95
- Federrath, C. & Klessen, R. S. 2012, ApJ, 761, 156
- Foster, J. B., Jackson, J. M., Barnes, P. J., et al. 2011, ApJS, 197, 25
- Gerin, M., Fossé, D., & Roueff, E. 2003, in SFChem 2002: Chemistry as a Diagnostic of Star Formation, ed. C. L. Curry & M. Fich, 81
- Goldsmith, P. F. 2001, ApJ, 557, 736
- Goldsmith, P. F. & Langer, W. D. 1978, ApJ, 222, 881
- Gong, M. & Ostriker, E. C. 2015, ApJ, 806, 31
- Graninger, D. M., Herbst, E., Öberg, K. I., & Vasyunin, A. I. 2014, ApJ, 787, 74
- Griffin, M. J., Abergel, A., Abreu, A., et al. 2010, A&A, 518, L3
- Harvey, P. M., Fallscheer, C., Ginsburg, A., et al. 2013, ApJ, 764, 133
- He, Y.-X., Zhou, J.-J., Esimbek, J., et al. 2015, MNRAS, 450, 1926
- Hennebelle, P. 2018, A&A, 611, A24
- Hildebrand, R. H. 1983, QJRAS, 24, 267
- Hirota, T., Yamamoto, S., Mikami, H., & Ohishi, M. 1998, ApJ, 503, 717
- Hony, S., Gouliermis, D. A., Galliano, F., et al. 2015, MNRAS, 448, 1847
- Hou, S., Jackson, J. M., Foster, J. B., et al. 2013, ApJ, 777, 157
- Irvine, W. M. & Schloerb, F. P. 1984, ApJ, 282, 516
- Jackson, J. M., Finn, S. C., Chambers, E. T., Rathborne, J. M., & Simon, R. 2010, ApJ, 719, L185
- Jiménez-Serra, I., Vasyunin, A. I., Caselli, P., et al. 2016, ApJ, 830, L6
- Kauffmann, J., Bertoldi, F., Bourke, T. L., Evans, II, N. J., & Lee, C. W. 2008, A&A, 487, 993
- Kauffmann, J., Pillai, T., Shetty, R., Myers, P. C., & Goodman, A. A. 2010, ApJ, 716, 433
- Keto, E. & Rybicki, G. 2010, ApJ, 716, 1315
- Klessen, R. S. 2001, ApJ, 556, 837
- Kong, S., Lada, C. J., Lada, E. A., et al. 2015, ApJ, 805, 58
- Könyves, V., André, P., Men'shchikov, A., et al. 2015, A&A, 584, A91
- Könyves, V., André, P., Men'shchikov, A., et al. 2010, A&A, 518, L106
- Kroupa, P. 2002, Science, 295, 82
- Kutner, M. L., Tucker, K. D., Chin, G., & Thaddeus, P. 1977, ApJ, 215, 521
- Lada, C. J., Lewis, J. A., Lombardi, M., & Alves, J. 2017, A&A, 606, A100
- Lada, C. J., Lombardi, M., & Alves, J. F. 2009, ApJ, 703, 52
- Lada, C. J., Lombardi, M., & Alves, J. F. 2010, ApJ, 724, 687

References

Alves, J., Lombardi, M., & Lada, C. J. 2007, A&A, 462, L17

- Lada, C. J., Muench, A. A., Rathborne, J., Alves, J. F., & Lombardi, M. 2008, *ApJ*, 672, 410
- Lang, K. R. 1980, *Science*, 207, 174
- Lewis, J. A. & Lada, C. J. 2016, *ApJ*, 825, 91
- Li, D. L., Esimbek, J., Zhou, J. J., et al. 2014, *A&A*, 567, A10
- Liu, H.-L., Wu, Y., Li, J., et al. 2015, *ApJ*, 798, 30
- Liu, T., Lacy, J., Li, P. S., et al. 2017, *ApJ*, 849, 25
- Liu, T., Wu, Y., & Zhang, H. 2012, *ApJS*, 202, 4
- Liu, X.-L., Wang, J.-J., & Xu, J.-L. 2013, *MNRAS*, 431, 27
- Loughnane, R. M., Redman, M. P., Thompson, M. A., et al. 2012, *MNRAS*, 420, 1367
- MacLaren, I., Richardson, K. M., & Wolfendale, A. W. 1988, *ApJ*, 333, 821
- Mangum, J. G. & Shirley, Y. L. 2015, *PASP*, 127, 266
- Mardones, D., Myers, P. C., Tafalla, M., et al. 1997, *ApJ*, 489, 719
- Men'shchikov, A. 2013, *A&A*, 560, A63
- Men'shchikov, A., André, P., Didelon, P., et al. 2010, *A&A*, 518, L103
- Men'shchikov, A., André, P., Didelon, P., et al. 2012, *A&A*, 542, A81
- Motte, F., Nony, T., Louvet, F., et al. 2018, *Nature Astronomy*, 2, 478
- Nutter, D. & Ward-Thompson, D. 2007, *MNRAS*, 374, 1413
- Padoan, P., Haugbølle, T., Nordlund, Å., & Frimann, S. 2017, *ApJ*, 840, 48
- Padoan, P. & Nordlund, Å. 2011, *ApJ*, 741, L22
- Padovani, M., Walmsley, C. M., Tafalla, M., Galli, D., & Müller, H. S. P. 2009, *A&A*, 505, 1199
- Padovani, M., Walmsley, C. M., Tafalla, M., Hily-Blant, P., & Pineau Des Forets, G. 2011, *A&A*, 534, A77
- Palmeirim, P., André, P., Kirk, J., et al. 2013, *A&A*, 550, A38
- Parikka, A., Juvela, M., Pelkonen, V.-M., Malinen, J., & Harju, J. 2015, *A&A*, 577, A69
- Pavlyuchenkov, Y., Wiebe, D., Shustov, B., et al. 2008, *ApJ*, 689, 335
- Poglitsch, A., Waelkens, C., Geis, N., et al. 2010, *A&A*, 518, L2
- Rivera-Ingraham, A., Martin, P. G., Polychroni, D., et al. 2013, *ApJ*, 766, 85
- Saltzeter, E. E. 1955, *ApJ*, 121, 161
- Sanhueza, P., Jackson, J. M., Foster, J. B., et al. 2012, *ApJ*, 756, 60
- Savage, C., Apponi, A. J., Ziurys, L. M., & Wyckoff, S. 2002, *ApJ*, 578, 211
- Schilke, P., Walmsley, C. M., Pineau Des Forets, G., et al. 1992, *A&A*, 256, 595
- Schneider, F. R. N., Sana, H., Evans, C. J., et al. 2018, *Science*, 361, aat7032
- Semenov, D., Hersant, F., Wakelam, V., et al. 2010, *A&A*, 522, A42
- Shadmehri, M. 2004, *MNRAS*, 354, 375
- Shirley, Y. L. 2015, *PASP*, 127, 299
- Stahler, S. W. 1984, *ApJ*, 281, 209
- Turner, B. E. 1995, *ApJ*, 449, 635
- Turner, B. E., Pirogov, L., & Minh, Y. C. 1997, *ApJ*, 483, 235
- Ungerechts, H., Bergin, E. A., Goldsmith, P. F., et al. 1997, *ApJ*, 482, 245
- Vasyunin, A. I., Caselli, P., Dulieu, F., & Jiménez-Serra, I. 2017, *ApJ*, 842, 33
- Vasyunin, A. I. & Herbst, E. 2013, *ApJ*, 762, 86
- Vasyunin, A. I., Semenov, D., Henning, T., et al. 2008, *ApJ*, 672, 629
- Vasyunin, A. I., Semenov, D. A., Wiebe, D. S., & Henning, T. 2009, *ApJ*, 691, 1459
- Vasyunin, A. I., Sobolev, A. M., Wiebe, D. S., & Semenov, D. A. 2004, *Astronomy Letters*, 30, 566
- Wakelam, V. & Herbst, E. 2008, *ApJ*, 680, 371
- Wakelam, V., Herbst, E., Le Bourlot, J., et al. 2010, *A&A*, 517, A21
- Wakelam, V., Herbst, E., & Selsis, F. 2006, *A&A*, 451, 551
- Wakelam, V., Selsis, F., Herbst, E., & Caselli, P. 2005, *A&A*, 444, 883
- Weisz, D. R., Johnson, L. C., Foreman-Mackey, D., et al. 2015, *ApJ*, 806, 198
- Williams, D. A. 1993, in *Reviews in Modern Astronomy*, Vol. 6, *Reviews in Modern Astronomy*, ed. G. Klare, 49–68
- Williams, J. P., Blitz, L., & Stark, A. A. 1995, *ApJ*, 451, 252
- Wilson, T. L. 1999, *Reports on Progress in Physics*, 62, 143
- Wu, Y., Liu, T., Meng, F., et al. 2012, *ApJ*, 756, 76
- Xu, J.-L., Xu, Y., Zhang, C.-P., et al. 2018, *A&A*, 609, A43
- Yuan, J., Wu, Y., Liu, T., et al. 2016, *ApJ*, 820, 37
- Muench, A. A., Lada, E. A., Lada, C. J., & Alves, J. 2002, *ApJ*, 573, 366

Table 1. IRAM 30m observed positions.

No.	R.A. (J2000)	DEC. (J2000)	T _{dust} (K)	Σ_{H_2} (10^{21} cm^{-2})	R (pc)	n(H ₂) (10^5 cm^{-3})	M (M _⊙)	M_V (M _⊙)	M_{BE} (M _⊙)	Type	Note
CMC-1	4h10m41.400s	38d07m59.00s	16.7	35.6	0.03	4.6	5.0	2.9	0.7	PRO	CMCHerschel-54
CMC-2	4h18m21.300s	38d01m36.00s	15.1	13.2	-	-	-	-	-	Galaxy	-
CMC-3	4h19m27.600s	38d00m03.00s	12.5	22.9	0.07	1.1	13.1	2.4	1.5	PRE	CMCHerschel-75
CMC-4	4h19m29.400s	37d59m43.00s	12.4	24.6	-	-	-	-	-	REF	-
CMC-5	4h21m38.500s	37d33m54.00s	12.9	23.7	-	-	-	-	-	REF	-
CMC-6	4h21m17.400s	37d33m16.00s	12.6	21.3	0.06	1.2	8.2	4.9	1.2	PRE	CMCHerschel-90
CMC-7	4h25m03.636s	37d16m28.83s	12.5	23.6	0.06	1.0	7.2	2.5	1.3	PRE	CMCHerschel-111
CMC-8	4h25m15.506s	37d11m44.89s	12.8	20.2	0.08	0.4	5.9	5.4	1.6	PRE	CMCHerschel-119
CMC-9	4h25m38.700s	37d07m08.00s	12.8	39.1	0.08	2.0	32.9	3.7	1.7	PRO	CMCHerschel-121
CMC-10	4h27m04.955s	36d57m03.17s	13.3	14.5	0.06	0.5	2.6	2.4	1.1	PRE	CMCHerschel-127
CMC-11	4h27m30.543s	36d49m26.77s	13.2	15.5	0.05	0.8	3.6	1.9	1.1	PRE	CMCHerschel-135
CMC-12	4h28m37.500s	36d25m27.00s	13.2	21.6	0.08	0.6	7.0	2.9	1.5	PRO	CMCHerschel-160
CMC-13	4h29m56.627s	36d09m56.60s	14.5	5.1	-	-	-	-	-	REF	-
CMC-14	4h30m17.258s	35d59m42.11s	13.7	7.3	-	-	-	-	-	REF	-
CMC-15	4h30m46.298s	35d59m16.50s	14.0	6.7	-	-	-	-	-	REF	-
CMC-16	4h30m37.600s	35d54m36.00s	12.8	46.3	0.07	1.8	15.3	5.0	1.3	PRO	CMCHerschel-197
CMC-17	4h30m39.200s	35d50m22.00s	13.1	35.4	0.04	4.3	6.5	2.4	0.7	PRO	CMCHerschel-205
CMC-18	4h30m31.300s	35d44m49.00s	12.6	17.1	0.03	2.3	2.8	5.2	0.7	PRO	CMCHerschel-215
CMC-19	4h30m47.800s	35d37m26.00s	13.2	14.9	0.05	2.1	8.5	2.7	1.0	PRO	CMCHerschel-225
CMC-20	4h30m41.400s	35d29m58.00s	12.8	46.3	0.08	1.0	16.8	4.8	1.7	PRO	CMCHerschel-232
CMC-21	4h30m40.800s	35d29m04.00s	13.1	34.1	0.05	2.6	8.7	3.1	1.0	PRE	CMCHerschel-235
CMC-22	4h30m16.000s	35d16m57.00s	34.9	11.2	-	-	-	-	-	REF	-
CMC-23	4h30m14.385s	35d16m25.75s	34.1	9.8	-	-	-	-	-	REF	-
CMC-24	4h30m25.600s	35d15m07.00s	26.2	6.2	-	-	-	-	-	REF	-
CMC-25	4h30m03.563s	35d14m13.88s	23.1	17.5	0.05	0.8	2.8	1.8	1.0	PRO	CMCHerschel-262
CMC-26	4h30m08.477s	35d14m01.69s	25.0	12.1	0.03	0.7	0.7	4.4	0.6	PRO	CMCHerschel-264
CMC-27	4h30m14.397s	35d13m31.85s	24.4	9.6	-	-	-	-	-	REF	-
CMC-28	4h30m28.400s	35d09m27.00s	16.2	28.1	-	-	-	-	-	REF	-
CMC-29	4h30m48.500s	34d58m37.00s	13.1	57.8	0.03	12.7	12.0	1.5	0.6	PRO	CMCHerschel-290
CMC-30	4h30m58.187s	34d53m36.72s	12.8	14.5	0.05	1.2	5.9	1.4	1.1	PRO	CMCHerschel-296

Notes.

R.A. and DEC are for the single-pointing observation positions.

T_{dust} is the dust average temperature in one beam (29'', IRAM 30m 86 GHz). Σ_{H_2} is the H₂ average column density in one beam.

CMC-2 is galaxy 3C111.

M is the Herschel core mass. M_{BE} is the Herschel core critical Bonnor-Ebert mass.

PRE is the gravitationally bound prestellar core. PRO is the protostellar core.

REF is the reference position that is offset from the cores.

We list the corresponding Herschel core in the notes.

Table 2. FELLWALKER configuration parameter values

Name	Explanation	Value
RMS estimated at the region without sources	5 × 10 ²⁰	
NOISE noise level	RMS	
FLATSLOPE change the route gradient	RMS	
MINDIP minimum dip between two adjacent cores	1.5*RMS	
MINHEIGHT minimum peak amplitude of a core	3*RMS	
FWHMBEAM beam at Herschel 250 μm , in pixels	3.64	
ALLOWEDGE cores are rejected at edge of the data	0	
CLEANITER cleans up core edge	5	
MINPIX minimum pixel value in a core	10	

Notes. We list the parameters changed from the default values recommended by FELLWALKER

No.	R.A. (J2000)	DEC. (J2000)	L_{maj} ('')	L_{min} ('')	θ ($^{\circ}$)	R_{eff} (pc)	T_{dust} (K)	$n(\text{H}_2)$ (10^5 cm^{-3})	M (M_{\odot})	M_{BE} (M_{\odot})	Type
CMCHerschel-271	04:30:15.573	+35:12:04.36	62.7	22.9	161.6	0.03	16.5	4.4	4.0	0.6	PRE
CMCHerschel-272	04:30:52.976	+35:11:35.49	28.9	19.4	78.6	0.01	15.9	3.2	0.2	0.3	USL
CMCHerschel-273	04:30:11.902	+35:10:57.55	69.1	25.2	176.6	0.04	16.4	1.1	1.7	0.7	PRE
CMCHerschel-274	04:30:26.045	+35:10:05.81	83.9	21.9	8.6	0.03	15.5	3.4	4.0	0.7	PRE
CMCHerschel-275	04:30:20.493	+35:09:25.78	87.0	26.6	152.6	0.04	14.8	1.4	3.6	0.9	PRE
CMCHerschel-276	04:30:28.654	+35:09:11.42	57.5	21.3	126.6	0.03	15.7	8.8	4.9	0.5	PRO
CMCHerschel-277	04:30:35.663	+35:08:56.04	37.1	24.7	150.6	0.03	15.1	1.3	0.6	0.5	PRE
CMCHerschel-278	04:30:40.950	+35:08:39.23	155.7	22.8	152.6	0.05	16.4	0.1	0.5	1.0	USL
CMCHerschel-279	04:30:27.433	+35:08:31.45	33.4	20.9	3.6	0.02	15.8	0.9	0.2	0.4	USL
CMCHerschel-280	04:30:50.826	+35:08:26.24	63.1	20.7	160.7	0.03	15.5	0.4	0.2	0.5	USL
CMCHerschel-281	04:30:22.339	+35:08:13.03	111.1	33.3	175.6	0.06	15.6	0.2	1.5	1.2	PRE
CMCHerschel-282	04:30:14.149	+35:07:41.34	89.0	25.7	6.6	0.04	14.8	0.9	2.0	0.9	PRE
CMCHerschel-283	04:30:08.405	+35:07:36.48	43.9	23.2	120.5	0.03	15.7	0.8	0.4	0.5	USL
CMCHerschel-284	04:30:37.011	+35:05:42.65	82.3	28.9	59.6	0.05	14.7	0.2	0.5	0.9	USL
CMCHerschel-285	04:30:26.986	+35:05:30.70	120.3	52.6	132.6	0.08	14.6	0.1	1.9	1.7	PRE
CMCHerschel-286	04:30:43.136	+35:05:30.04	85.6	22.6	92.6	0.04	15.3	0.1	0.2	0.7	USL
CMCHerschel-287	04:30:22.399	+35:04:33.74	70.8	26.7	50.6	0.04	14.4	0.6	1.0	0.8	PRE
CMCHerschel-288	04:30:33.382	+35:03:35.79	94.1	20.1	123.6	0.03	14.7	0.3	0.3	0.6	USL
CMCHerschel-289	04:30:55.790	+34:59:22.17	37.9	24.5	56.7	0.03	14.7	0.5	0.2	0.5	USL
CMCHerschel-290	04:30:48.261	+34:58:36.98	88.9	20.7	138.6	0.03	13.0	12.7	12.0	0.6	PRO
CMCHerschel-291	04:30:39.207	+34:58:08.21	67.2	22.7	4.7	0.03	14.1	0.8	0.8	0.6	PRE
CMCHerschel-292	04:30:57.010	+34:57:22.94	83.4	28.6	171.7	0.05	13.7	0.5	1.4	0.9	PRE
CMCHerschel-293	04:30:54.183	+34:56:20.47	76.2	38.4	85.6	0.05	12.8	0.8	3.8	1.1	PRO
CMCHerschel-294	04:30:47.040	+34:56:11.00	49.9	26.3	170.7	0.03	14.4	0.4	0.4	0.6	USL
CMCHerschel-295	04:30:53.073	+34:55:19.45	43.3	26.3	173.7	0.03	12.4	3.7	2.8	0.6	PRE
CMCHerschel-296	04:30:57.614	+34:53:44.20	79.8	37.3	144.7	0.05	12.6	1.2	5.9	1.1	PRO
CMCHerschel-297	04:31:04.711	+34:53:07.61	65.1	33.0	70.7	0.05	14.5	0.2	0.5	0.9	USL
CMCHerschel-298	04:31:01.690	+34:50:54.31	78.4	34.2	122.7	0.05	14.1	0.3	1.0	1.0	PRE
CMCHerschel-299	04:31:25.834	+34:50:52.95	72.6	37.8	46.8	0.05	13.6	0.6	2.4	1.0	PRE
CMCHerschel-300	04:31:21.652	+34:47:45.70	43.8	23.9	75.7	0.03	15.1	0.8	0.5	0.5	USL

Table 3 — Continued

Table 4. Properties of molecular lines.

H ¹³ CO ⁺ J = 1 – 0							
No.	T _{mb} (K)	∫ T _{mb} dv (K km s ⁻¹)	FWHM (km s ⁻¹)	V _{LSR} (km s ⁻¹)	τ	N (10 ¹² cm ⁻²)	X (10 ⁻¹¹)
CMC-1	1.18(0.05)	0.87(0.05)	0.69(0.49)	-3.63(0.09)	0.21	2.47	3.47
CMC-2	-	-	-	-	-	-	-
CMC-3	0.58(0.05)	0.41(0.08)	0.68(7.10)	-2.40(0.03)	-	-	-
CMC-4	0.45(0.05)	0.33(0.05)	0.67(0.81)	-2.28(0.05)	-	-	-
CMC-5	0.58(0.05)	0.60(0.06)	0.98(0.11)	-1.23(0.06)	-	-	-
CMC-6	0.24(0.05)	0.26(0.07)	1.03(0.41)	-0.21(0.16)	0.19	0.32	0.76
CMC-7	0.66(0.04)	0.47(0.05)	0.67(1.75)	-1.78(0.05)	-	-	-
CMC-8	0.50(0.05)	0.53(0.06)	1.00(0.12)	-2.57(0.07)	0.81	0.62	1.54
CMC-9	0.75(0.05)	0.66(0.06)	0.83(0.20)	-1.72(0.05)	-	-	-
CMC-10	0.29(0.05)	0.21(0.04)	0.67(0.17)	-1.88(0.13)	-	-	-
CMC-11	-	-	-	-	-	-	-
CMC-12	1.07(0.05)	0.80(0.05)	0.71(0.36)	-1.45(0.09)	-	-	-
CMC-13	-	-	-	-	-	-	-
CMC-14	-	-	-	-	-	-	-
CMC-15	0.24(0.05)	0.18(0.06)	0.70(0.45)	-1.22(0.22)	0.22	0.40	3.01
CMC-16	1.15(0.05)	1.43(0.07)	1.17(0.07)	-1.43(0.03)	0.59	4.19	4.52
CMC-17	0.61(0.05)	0.67(0.06)	1.04(0.11)	-1.36(0.05)	0.23	1.36	1.92
CMC-18	0.77(0.04)	0.83(0.05)	1.01(0.07)	-1.79(0.03)	0.51	1.80	5.27
CMC-19	0.57(0.05)	0.41(0.07)	0.67(3.27)	-0.91(0.03)	0.83	1.31	4.41
CMC-20	0.89(0.05)	0.79(0.06)	0.84(0.06)	-0.64(0.04)	0.31	1.25	1.35
CMC-21	0.52(0.04)	0.38(0.04)	0.67(0.41)	-0.69(0.06)	0.71	0.97	1.43
CMC-22	-	-	-	-	-	-	-
CMC-23	-	-	-	-	-	-	-
CMC-24	-	-	-	-	-	-	-
CMC-25	0.44(0.05)	0.37(0.06)	0.80(0.11)	-0.55(0.09)	0.28	2.32	6.62
CMC-26	-	-	-	-	-	-	-
CMC-27	-	-	-	-	-	-	-
CMC-28	0.61(0.05)	0.87(0.07)	1.34(0.14)	0.51(0.06)	0.22	1.71	3.05
CMC-29	0.67(0.05)	0.64(0.06)	0.90(0.09)	-0.67(0.05)	0.42	1.52	1.32
CMC-30	0.59(0.05)	0.42(0.06)	0.68(0.45)	-0.54(0.11)	1.37	1.45	5.02

Notes. T_{mb} is the corrected main-beam temperature. $\int T_{mb} dv$ is the integrated main-beam temperature T_{mb} .

FWHM is the full width at half-maximum of the Gaussian fitting profile of the molecular line.

The FWHM of HCN(1 – 0) is the main component JF = (12 – 01).

The FWHM of N₂H⁺(1 – 0) is its first component JF₁F = (101 – 012). V_{LSR} is the local standard of rest velocity. N is the column density. X is the abundance. N and X for HCN and N₂H⁺ are derived from their component JF = (12 – 01) and JF₁F = (101 – 012), respectively.Optical depth τ for C₂H is estimated by its main component JF = (3/2, 2 – 1/2, 1) with the HFS method in the CLASS software.Optical depth τ for HCN is estimated by its main component JF = (12 – 01).Optical depth τ for N₂H⁺ is estimated by its first component JF₁F = (101 – 012)

Table 5. Detection rates of the observed molecular lines ($J = 1 - 0$) for 14 protostellar cores, 7 prestellar cores, and 8 observation reference positions that are offset from the cores.

No.	H ¹³ CO ⁺	HN ¹³ C	C ₂ H	HCN	HCO ⁺	HNC	N ₂ H ⁺	C ¹⁸ O	¹³ CO
Protostellar	79%	64%	100%	100%	100%	100%	71%	86%	100%
Prestellar	86%	71%	71%	71%	57%	71%	71%	100%	100%
Reference	50%	13%	88%	88%	88%	100%	38%	100%	100%

Table 6. Parameters used to calculate the molecular column densities.

Line Name	ν (MHz)	E_u/k (K)	μ (D)	B_0 (MHz)	R_i
H ¹³ CO ⁺ (1 - 0)	86754.288	4.16	3.90	43377.3	1
HN ¹³ C (1 - 0)	87090.851	4.18	2.699	43545.61	1
C ₂ H (1 - 0)	87316.898	4.19	0.769	43674.52	0.416 ^a
HCN (1 - 0)	88631.847	4.25	2.984	44315.97	5/9 ^b
HCO ⁺ (1 - 0)	89188.526	4.28	3.888	44594.4	1
HNC (1 - 0)	90663.568	4.35	3.05	45331.98	1
N ₂ H ⁺ (1 - 0)	93173.777	4.47	3.40	46586.87	1/9 ^c
C ¹⁸ O (1 - 0)	109782.176	5.27	0.11049	54891.42	1
¹³ CO (1 - 0)	110201.3543	5.29	0.11046	55101.01	1

Notes. ν is the rest frequency. E_u is the upper energy. k is the Boltzmann constant. μ is the permanent dipole moment along the axis of symmetry. B_0 is the rigid rotor rotation constant. R_i is the relative intensity.a: The relative intensity for C₂H JF = (3/2, 2 - 1/2, 1).b: The relative intensity for N₂H⁺ JF₁F = (101 - 012).

c: The relative intensity for HCN JF = (12 - 01).

Table 7. Statistics of abundance ratios of 14 protostellar and 7 prestellar cores

	H^{13}CO^+ (10^{-11})	HN^{13}C (10^{-11})	C_2H (10^{-9})	HCN (10^{-9})	HCO^+ (10^{-9})	HNC (10^{-9})	N_2H^+ (10^{-10})	C^{18}O (10^{-8})	^{13}CO (10^{-6})
Max.	6.62	6.77	8.18	4.80	3.31	3.39	5.58	13.56	2.55
Min.	0.76	1.23	0.36	0.08	0.38	0.62	0.52	1.20	0.09
Mean	3.14	2.38	1.99	1.00	1.57	1.19	2.04	6.37	0.46
Median	2.69	1.97	1.55	0.40	1.35	0.99	1.67	5.99	0.21
Std.	1.98	1.49	1.92	1.35	0.99	0.75	1.52	3.67	0.60

Table 8. Molecular line skewed profile.

No.	V_{thick} $\text{HCO}^+(1 - 0)$ (km s $^{-1}$)	V_{thick} $\text{HNC}(1 - 0)$ (km s $^{-1}$)	V_{thin} $\text{C}^{18}\text{O}(1 - 0)$ (km s $^{-1}$)	ΔV $\text{C}^{18}\text{O}(1 - 0)$ (km s $^{-1}$)	δV $\text{HCO}^+(1 - 0)$	δV $\text{HNC}(1 - 0)$	Profile
CMC-1	-3.68(0.01)	-3.67(-3.67)	-3.63(0.04)	1.18(0.11)	-0.05(0.05)	-0.04(0.05)	N,N
CMC-2	-	-	-	-	-	-	-,-
CMC-3	-	-2.44(-2.44)	-2.33(0.02)	0.63(0.03)	-	-0.18(0.12)	-,N
CMC-4	-	-2.09(-2.09)	-2.24(0.02)	0.66(0.03)	-	0.23(0.16)	-,N
CMC-5	0.09(0.08)	-1.06(-1.06)	-1.21(0.01)	1.00(0.03)	1.30(0.13)	0.15(0.07)	R,N
CMC-6	-0.09(0.02)	-0.43(-0.43)	-0.46(0.02)	1.11(0.05)	0.33(0.05)	0.02(0.04)	R,N
CMC-7	-	-1.87(-1.87)	-1.77(0.02)	0.73(0.07)	-	-0.14(0.08)	-,N
CMC-8	-2.94(0.03)	-2.85(-2.85)	-2.34(0.02)	1.02(0.05)	-0.58(0.08)	-0.50(0.06)	B,B
CMC-9	-2.52(0.08)	-1.80(-1.80)	-1.83(0.01)	0.78(0.03)	-0.88(0.17)	0.04(0.08)	B,N
CMC-10	-	-	-1.81(0.01)	0.76(0.05)	-	-	-,-
CMC-11	-2.05(0.05)	-	-1.42(0.01)	0.68(0.02)	-0.92(0.11)	-	B,-
CMC-12	-1.67(0.04)	-1.48(-1.48)	-1.47(0.02)	0.71(0.03)	-0.27(0.09)	-0.01(0.06)	B,N
CMC-13	-0.58(0.13)	-0.19(-0.19)	-0.13(0.01)	0.53(0.06)	-0.84(0.38)	-0.11(0.21)	B,N
CMC-14	-1.08(0.04)	-0.98(-0.98)	-0.65(0.03)	0.88(0.06)	-0.49(0.11)	-0.37(0.10)	B,B
CMC-15	-1.17(0.03)	-1.04(-1.04)	-1.21(0.02)	0.83(0.07)	0.04(0.07)	0.20(0.08)	N,N
CMC-16	-1.16(0.02)	-1.19(-1.19)	-1.49(0.02)	1.07(0.04)	0.31(0.04)	0.28(0.04)	R,R
CMC-17	-1.87(0.02)	-1.50(-1.50)	-1.10(0.03)	0.98(0.07)	-0.78(0.10)	-0.40(0.07)	B,B
CMC-18	-1.84(0.02)	-1.88(-1.88)	-1.27(0.03)	1.57(0.07)	-0.36(0.05)	-0.39(0.05)	B,B
CMC-19	-0.96(0.04)	-0.79(-0.79)	-1.01(0.01)	0.87(0.02)	0.05(0.05)	0.25(0.07)	N,R
CMC-20	-0.49(0.01)	-0.54(-0.54)	-0.53(0.01)	0.93(0.02)	0.05(0.02)	-0.00(0.03)	N,N
CMC-21	-0.50(0.03)	-0.52(-0.52)	-0.61(0.01)	0.98(0.02)	0.10(0.05)	0.09(0.04)	N,N
CMC-22	-1.96(0.03)	-1.91(-1.91)	-	-	-	-	-,-
CMC-23	-1.44(0.03)	-1.13(-1.13)	-	-	-	-	-,-
CMC-24	0.07(0.04)	0.01(0.01)	-0.59(0.04)	0.73(0.06)	0.91(0.18)	0.84(0.33)	R,R
CMC-25	-0.46(0.02)	-0.61(-0.61)	-0.85(0.01)	0.72(0.05)	0.54(0.09)	0.33(0.07)	R,R
CMC-26	0.37(0.02)	0.10(0.10)	0.04(0.04)	1.52(0.10)	0.22(0.06)	0.04(0.05)	N,N
CMC-27	0.30(0.03)	0.13(0.13)	0.46(0.07)	1.31(0.17)	-0.12(0.09)	-0.26(0.12)	N,B
CMC-28	0.84(0.01)	0.74(0.74)	0.52(0.03)	1.38(0.08)	0.23(0.05)	0.16(0.05)	N,N
CMC-29	-0.51(0.02)	-0.54(-0.54)	-0.70(0.03)	0.80(0.07)	0.24(0.08)	0.21(0.07)	N,N
CMC-30	-0.47(0.04)	-0.41(-0.41)	-0.53(0.07)	0.53(0.27)	0.11(0.26)	0.23(0.27)	N,N

Notes. The $\text{HCO}^+(1 - 0)$ and $\text{HNC}(1 - 0)$ profiles are evaluated as follows: B denotes a blue profile. R denotes a red profile. N denotes neither blue nor red.

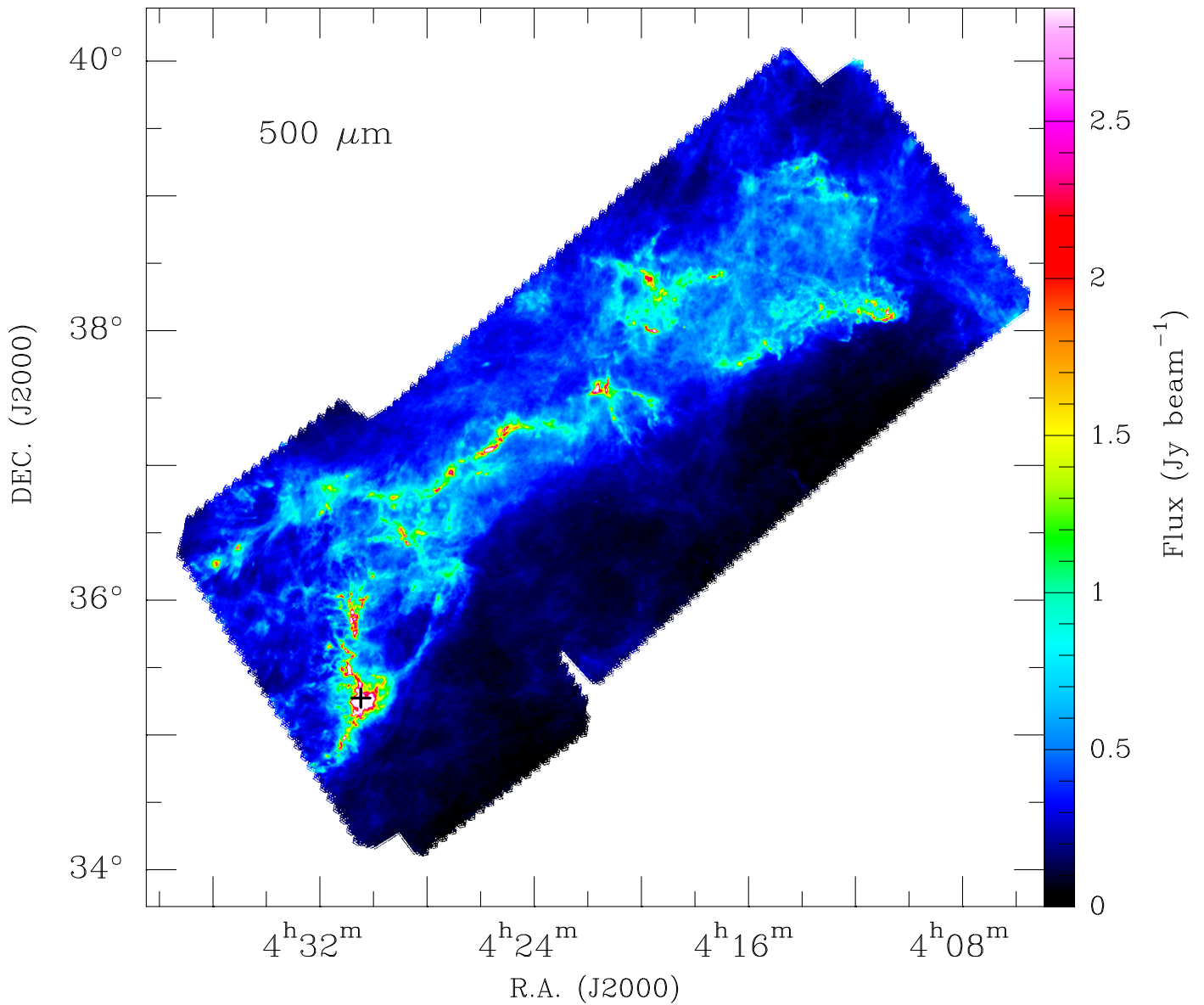


Fig. 1. California molecular cloud map at the Herschel 500 μm band. This map is shown from 0 to 20% of the peak value ($14.3 \text{ Jy beam}^{-1}$). The 500 μm beam is 36.3''. The area is about 18 deg². LkH α 101 is a B star, which is the brightest star in the CMC. It is located in the lower left corner and illuminates the surrounding gas. We mark this star with a black cross on the map.

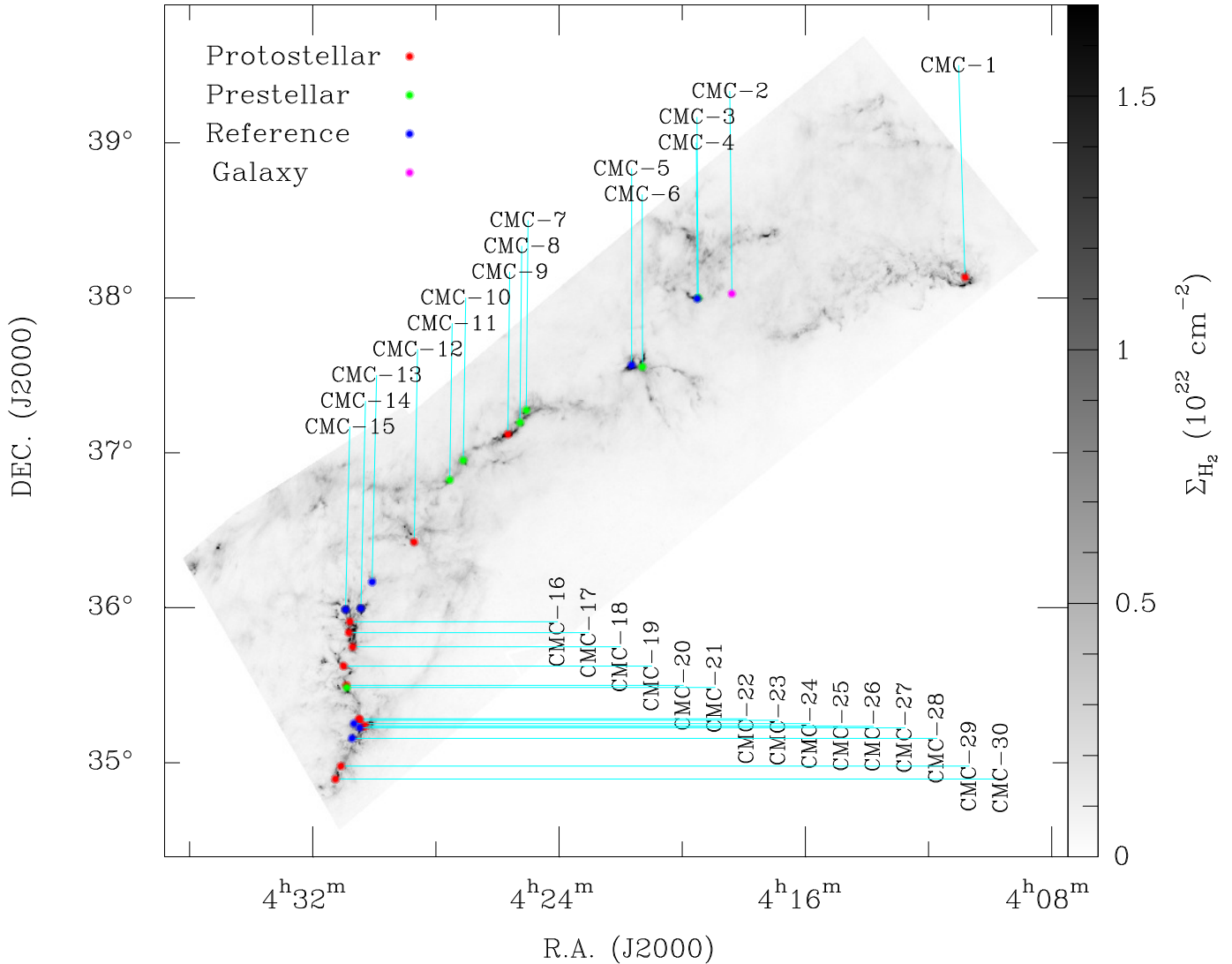


Fig. 2. Thirty positions for the IRAM 30m single-pointing observations on the Herschel H₂ column density map. This map is shown from 0 to 20% of the peak value ($8.4 \times 10^{22} \text{ cm}^{-2}$). The 500 μm beam is 36.3". The 30 observation positions are along the main filament in the CMC. The 14 protostellar cores are plotted with red solid circles, the seven prestellar cores are plotted with green solid circles, the eight observation positions are reference positions that are offset from the cores plotted with blue solid circles, and one position is projected on galaxy 3C111, plotted with pink solid circle.

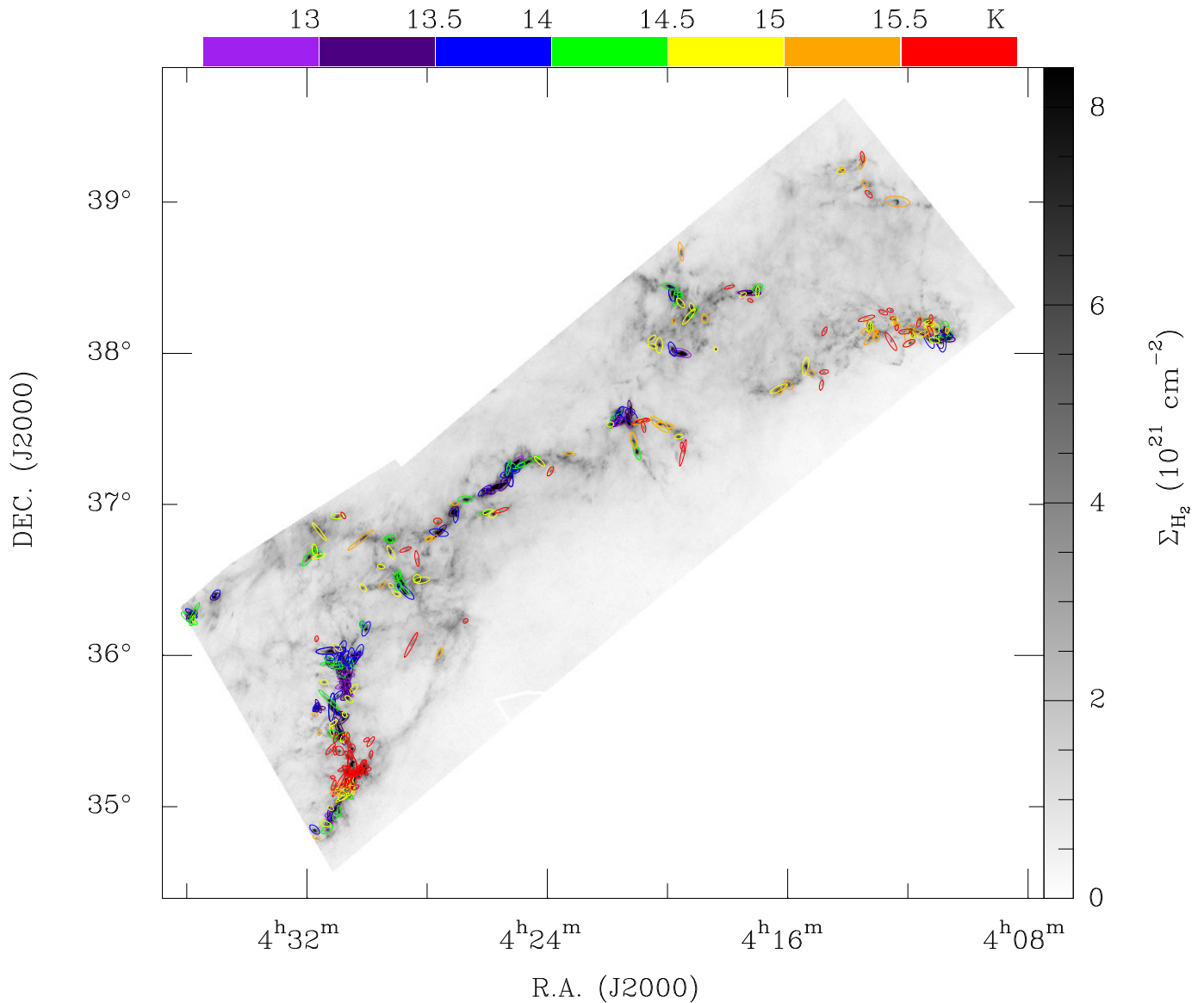


Fig. 3. Three hundred cores in the California molecular cloud plotted in the H_2 column density map. This map is shown from 0 to 10% of the peak value ($8.4 \times 10^{22} \text{ cm}^{-2}$). The cores are displayed with the measured dust temperature in units of K, coded as shown in the color bar on the top. The major and minor axes of the core ellipse shape in this map are 4 FWHMs of the equivalent Gaussian.

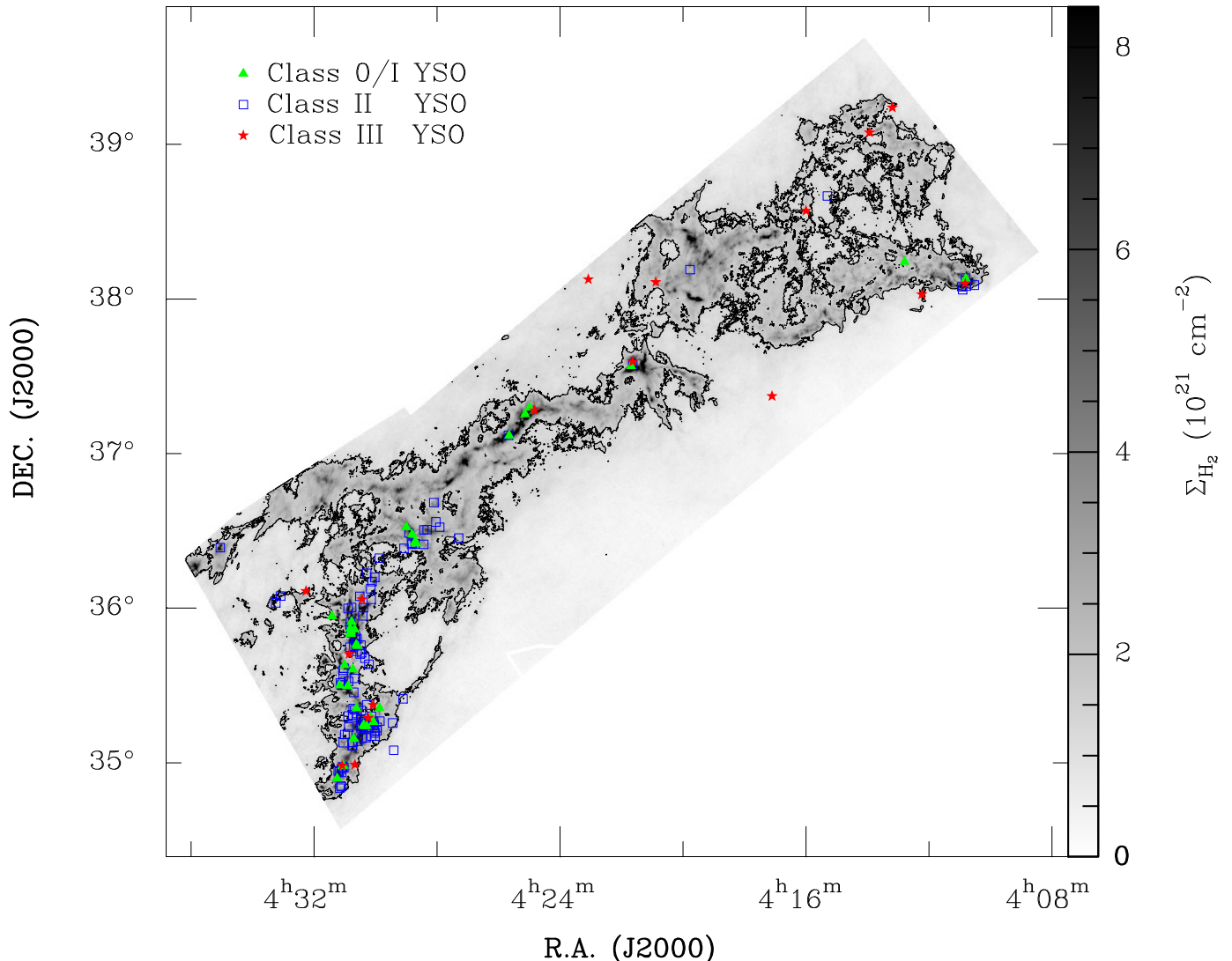


Fig. 4. Distribution of YSOs in the Herschel H₂ column density map. This map is shown from 0 to 10% of the peak value ($8.4 \times 10^{22} \text{ cm}^{-2}$). The noise σ is $0.5 \times 10^{21} \text{ cm}^{-2}$ estimated in the region from off-sources. The black contour is 3σ .

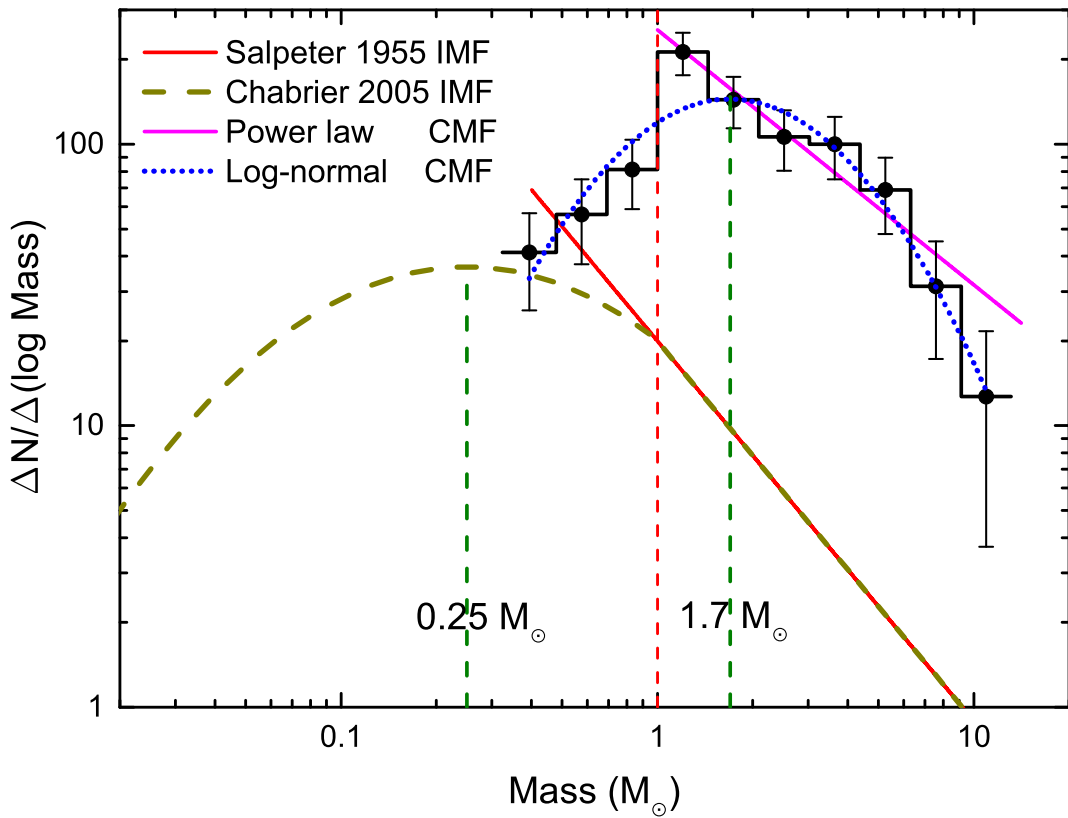


Fig. 5. Prestellar CMF fit by power law and log-normal distribution. The error bars correspond to \sqrt{N} statistical uncertainties. The bin of the prestellar CMF is 0.16 in logarithmic space. The number of the bin is 10. The bins start from $1 M_\odot$ to the high- and low-mass end. The prestellar CMF observed above $1 M_\odot$ can be fit by a power law with $dN/d\log M \propto M^{-0.9 \pm 0.1}$, which is shallower than the Salpeter 1955 IMF $dN/d\log M \propto M^{-1.35}$. The prestellar CMF can be well fit by a log-normal with $\mu = \log(1.7 \pm 0.1 M_\odot)$, $\sigma = 0.37 \pm 0.03$ in $\log(M_\odot)$ unit. $1.7 M_\odot$ is the log-normal fit peak value, which also corresponds to the log-normal fit average value, while σ is the standard deviation. The peak value of Chabrier 2005 is $0.25 M_\odot$. The prestellar CMF is similar to the IMF. The mass transformation efficiency ϵ from the prestellar core to the star is about $15 \pm 1\%$, as estimated by comparing the peak value between the CMC log-normal prestellar CMF and the Chabrier (2005) IMF.

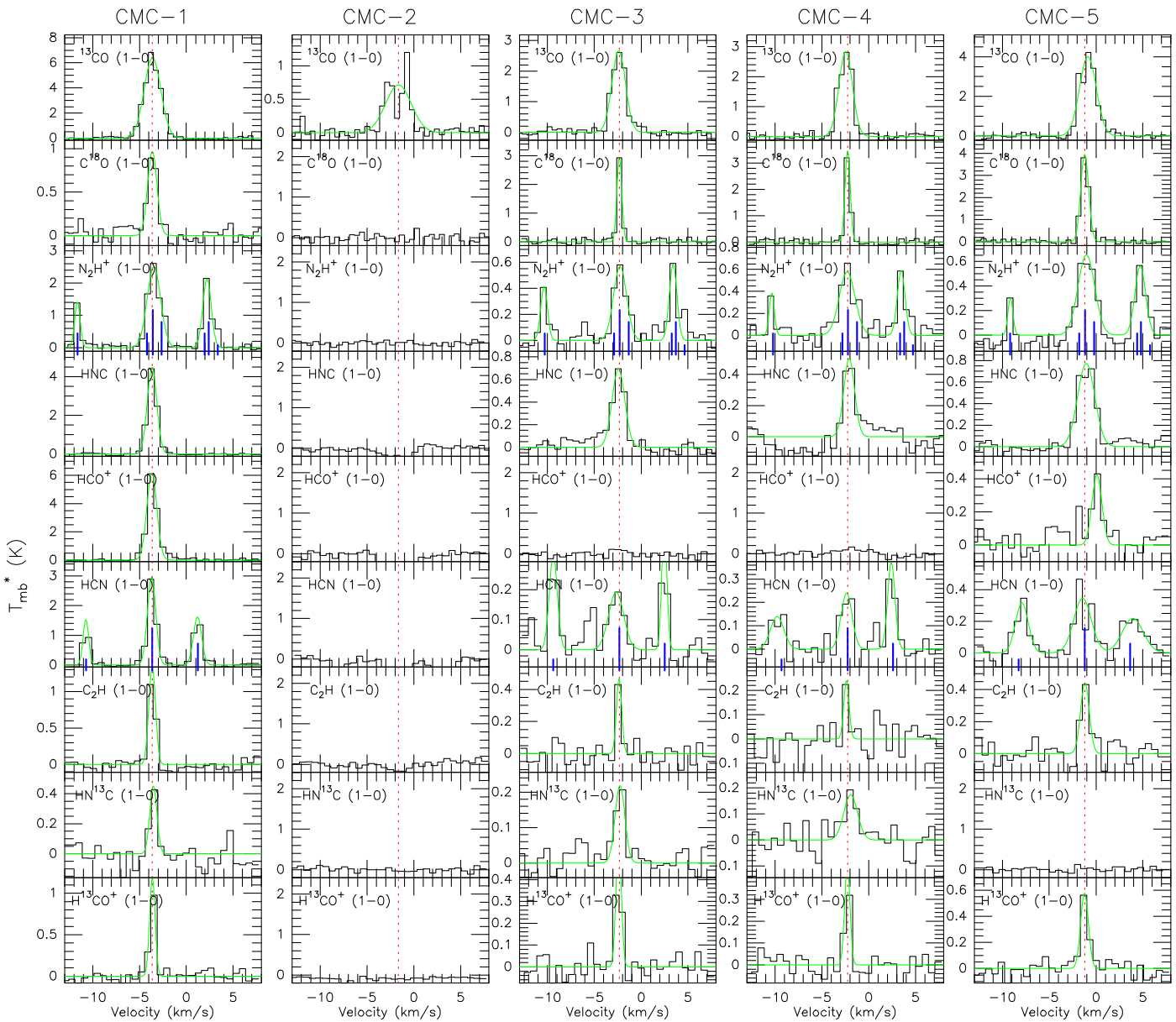


Fig. 6. Thirty molecular lines of the IRAM 30m observation point. The green curves indicate the Gauss-fit profile. The red dashed lines mark the position of the local standard of rest velocity. The blue lines mark the position of the $\text{N}_2\text{H}^+(1-0)$ and $\text{HCN}(1-0)$ hyperfine structure.

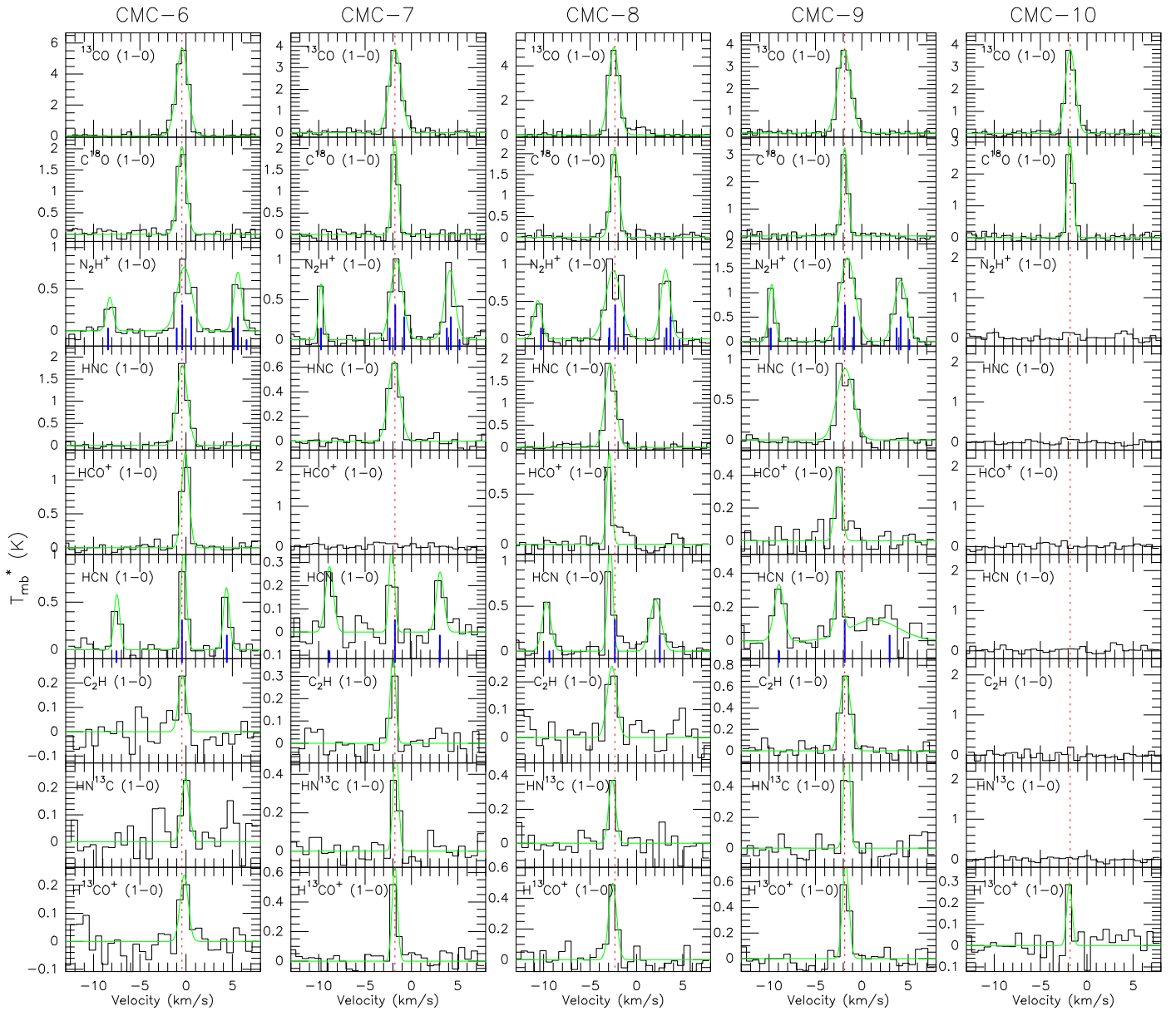


Fig. 6 — Continued

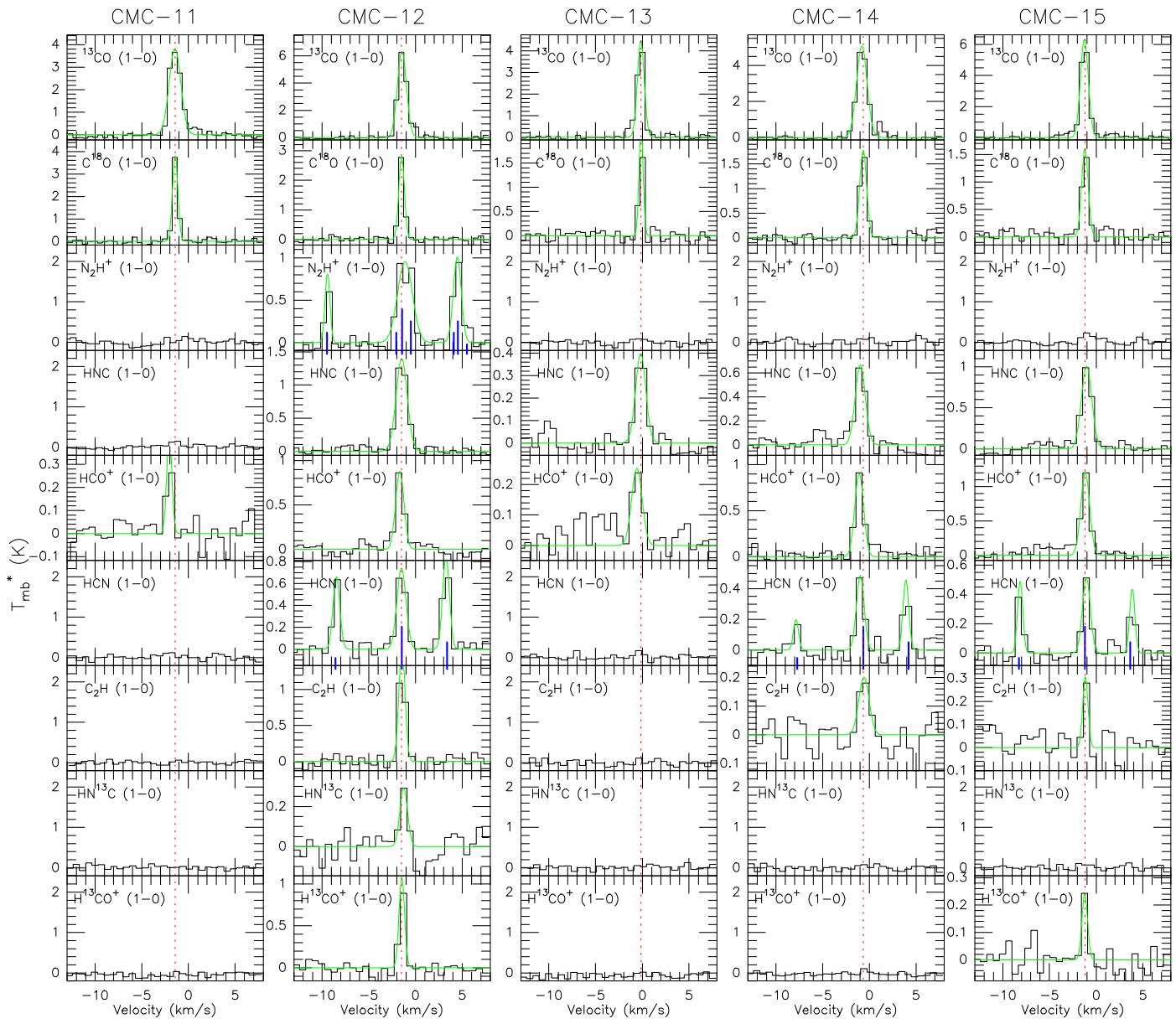


Fig. 6 — Continued

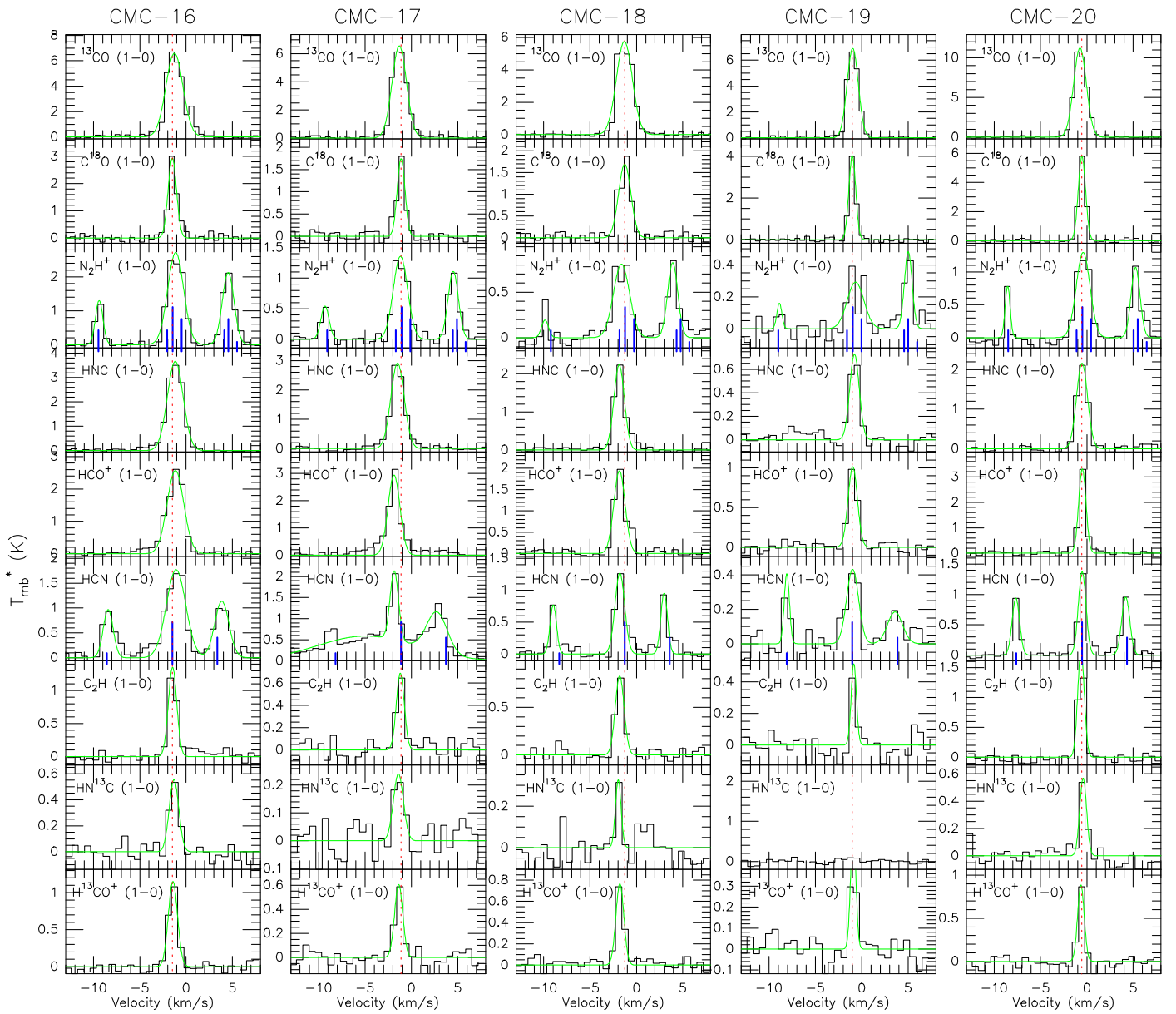


Fig. 6 — Continued

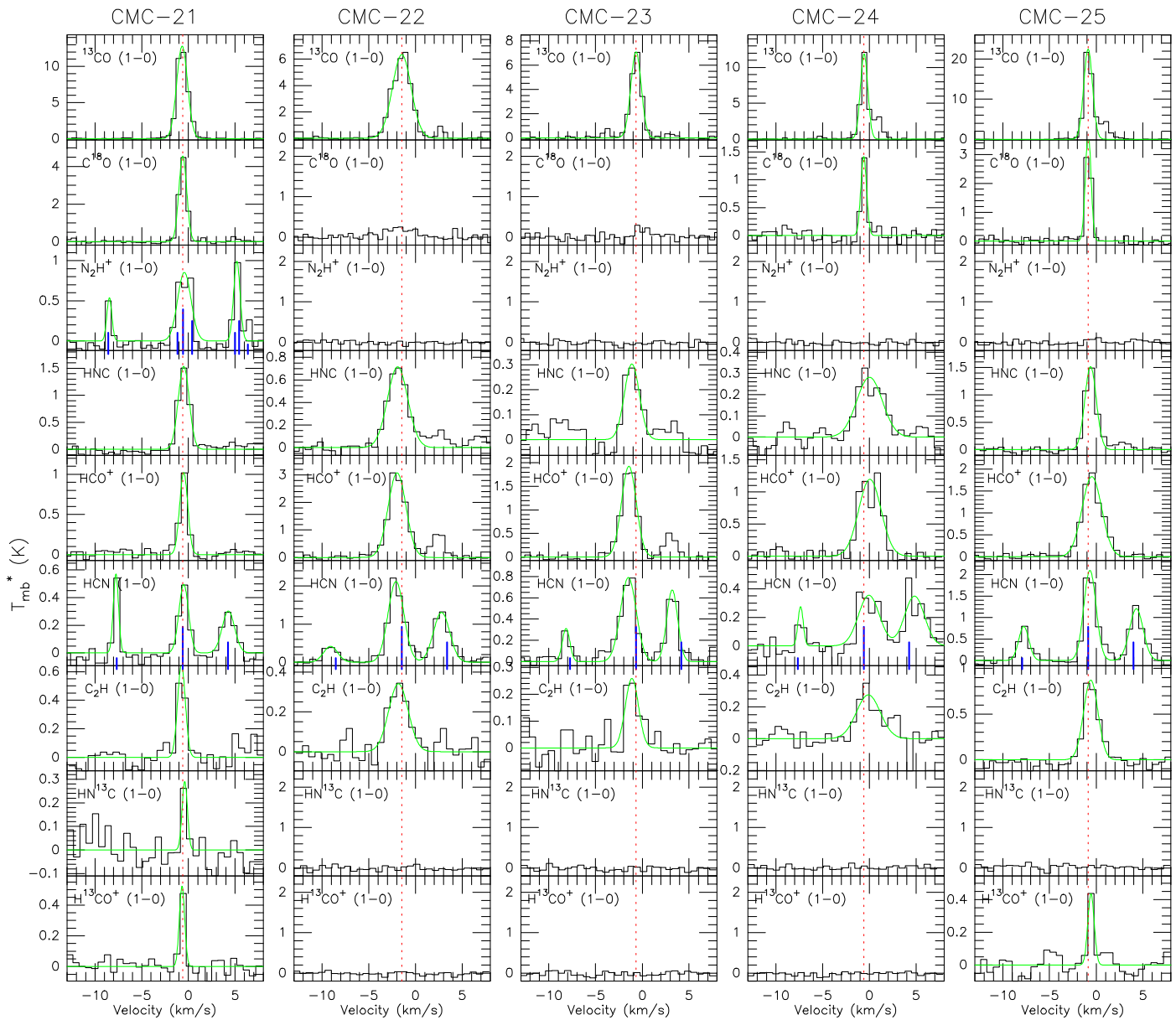


Fig. 6 — Continued

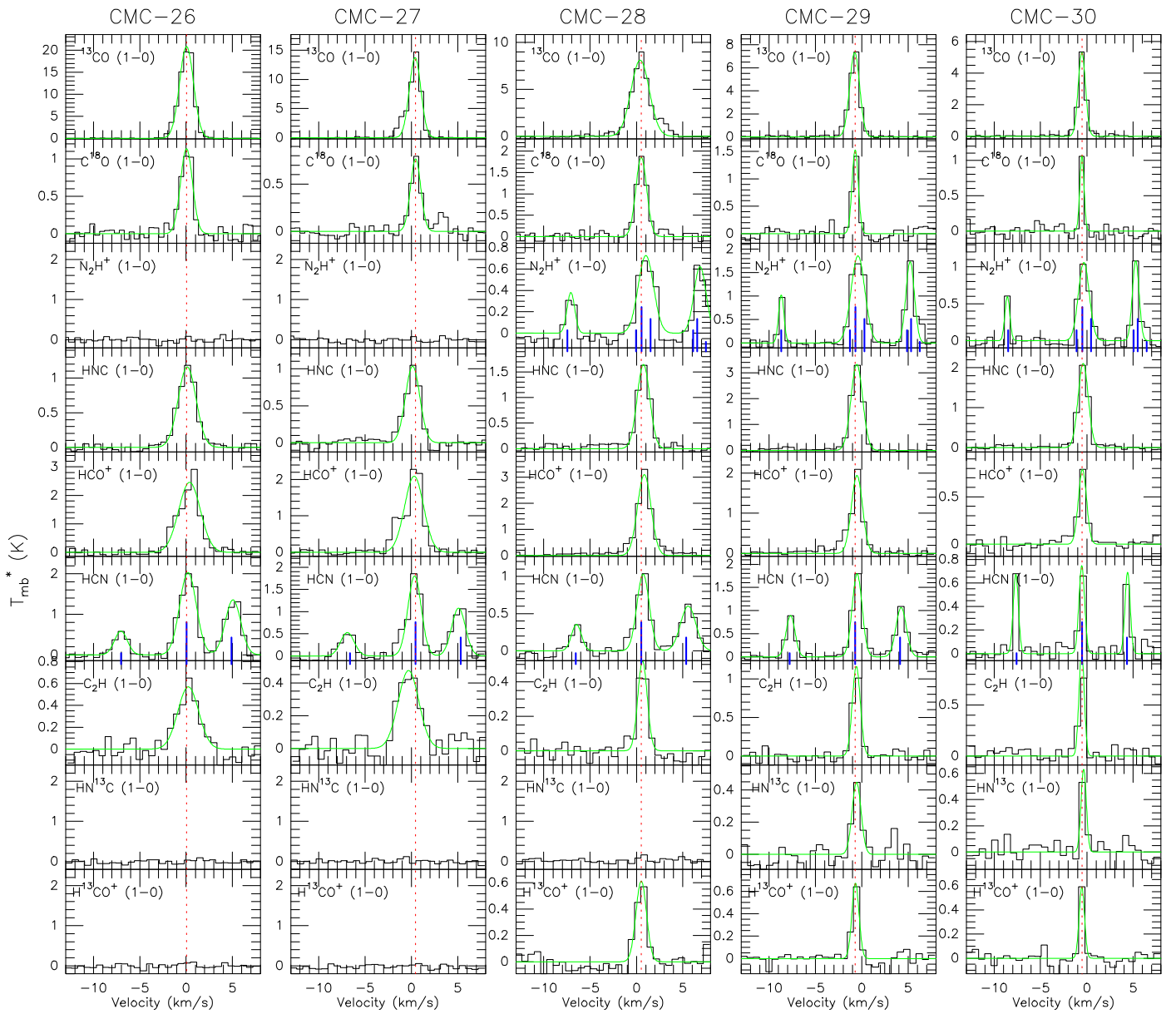


Fig. 6 — Continued

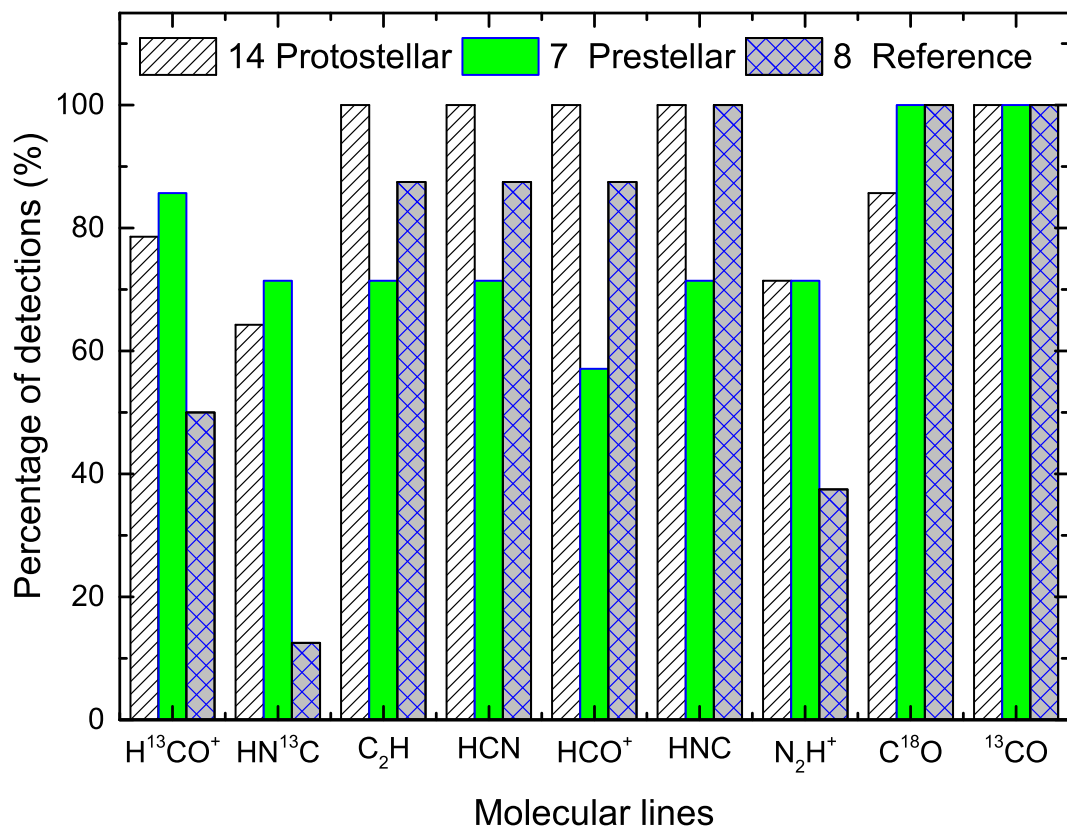


Fig. 7. Detection rates of the observed molecular lines ($J = 1 - 0$) toward 14 protostellar cores, 7 prestellar cores, and eight observation positions that are offset from cores.

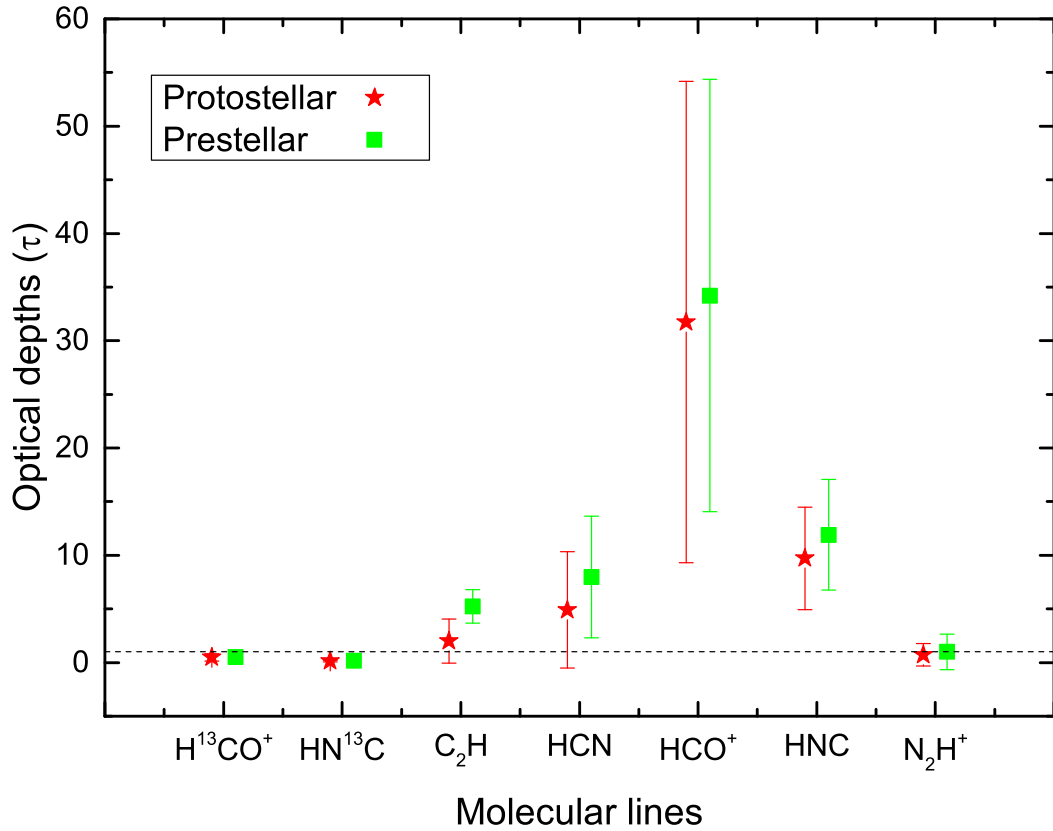


Fig. 8. Average optical depths (τ) of the observed molecular lines ($J = 1 - 0$). The protostellar cores are plotted with red stars and prestellar cores are shown with green squares. The dashed line shows $\tau = 1$.

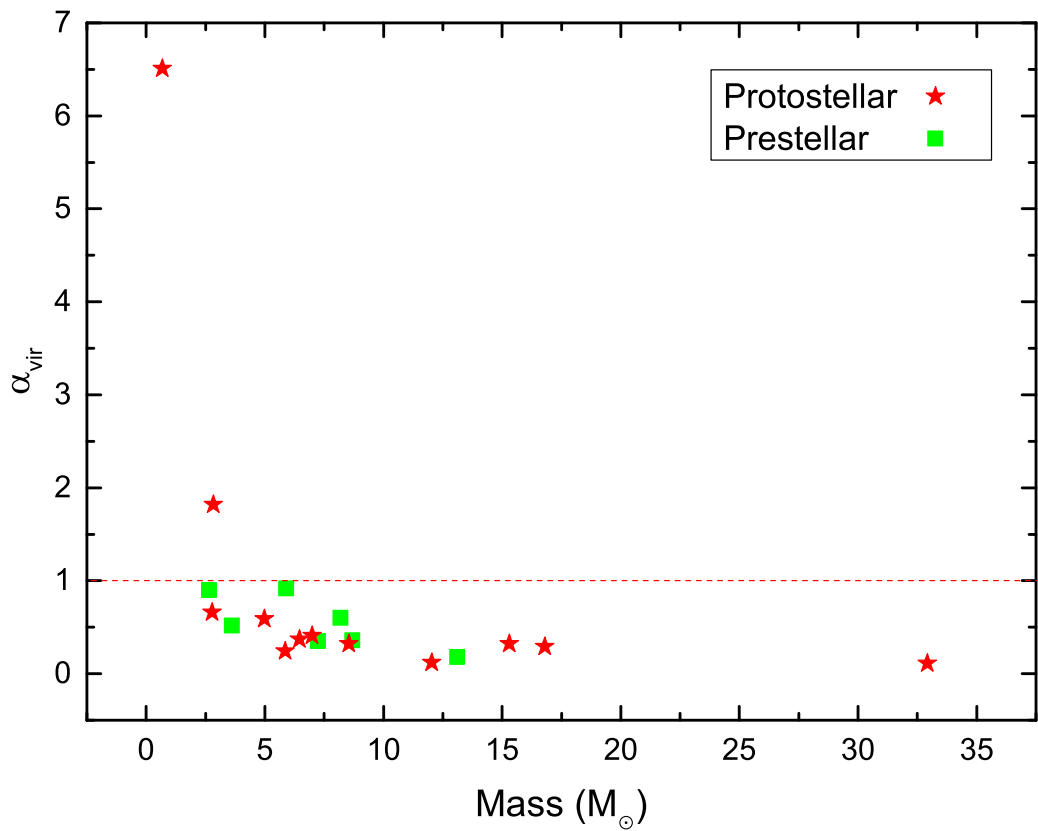


Fig. 9. C¹⁸O virial parameter α_{vir} vs. core masses for 12 protostellar cores (2 of 14 protostellar cores do not detect C¹⁸O) and seven prestellar cores.

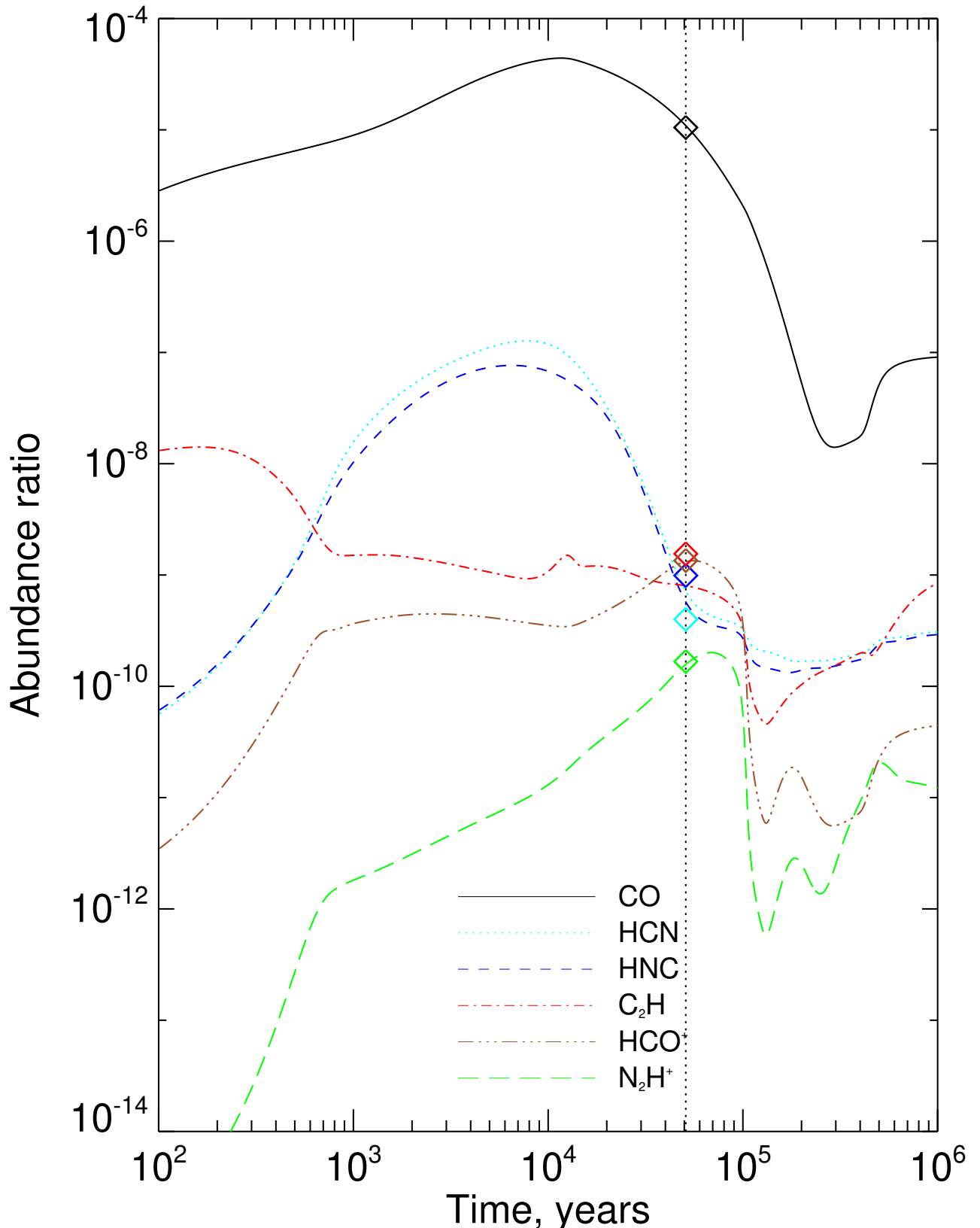


Fig. 10. Core chemical age. The colored diamonds indicate the average values of the observations from Table 7. The CO abundance is obtained from ^{13}CO by $[\text{CO}]/[^{13}\text{CO}] = 50$. The best agreement between the model and the median values of the observations is attained at $\sim 5 \times 10^4$ years.

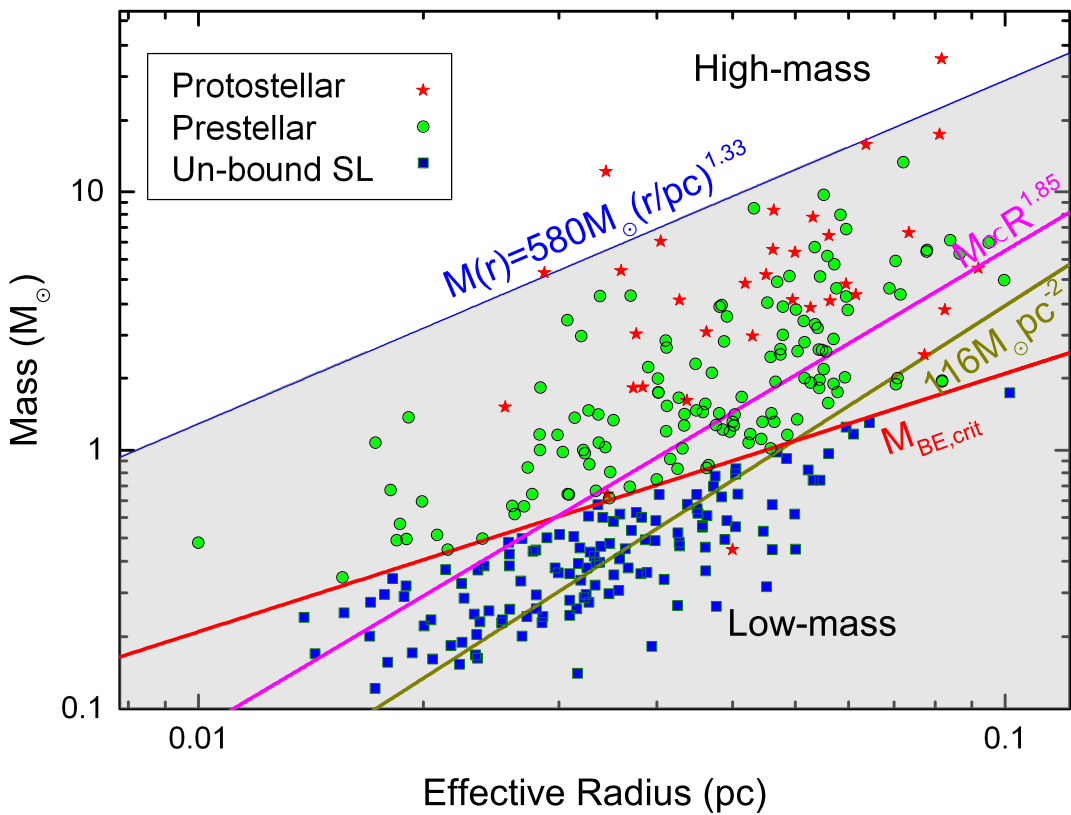


Fig. 11. Mass-radius relationship of cores. The red star, green circle, and blue square indicate protostellar, prestellar, and unbound starless cores, respectively. The pink line shows that the mass-radius relationship for all the cores can be well fit with a power law: $M \propto R^{1.85}$. The gray shaded region indicates that high-mass stars cannot form (Kauffmann et al. 2010). The green line presents surface densities of $116 M_{\odot} \text{ pc}^2$. The red line presents the surface density of the critical Bonnor-Ebert sphere.

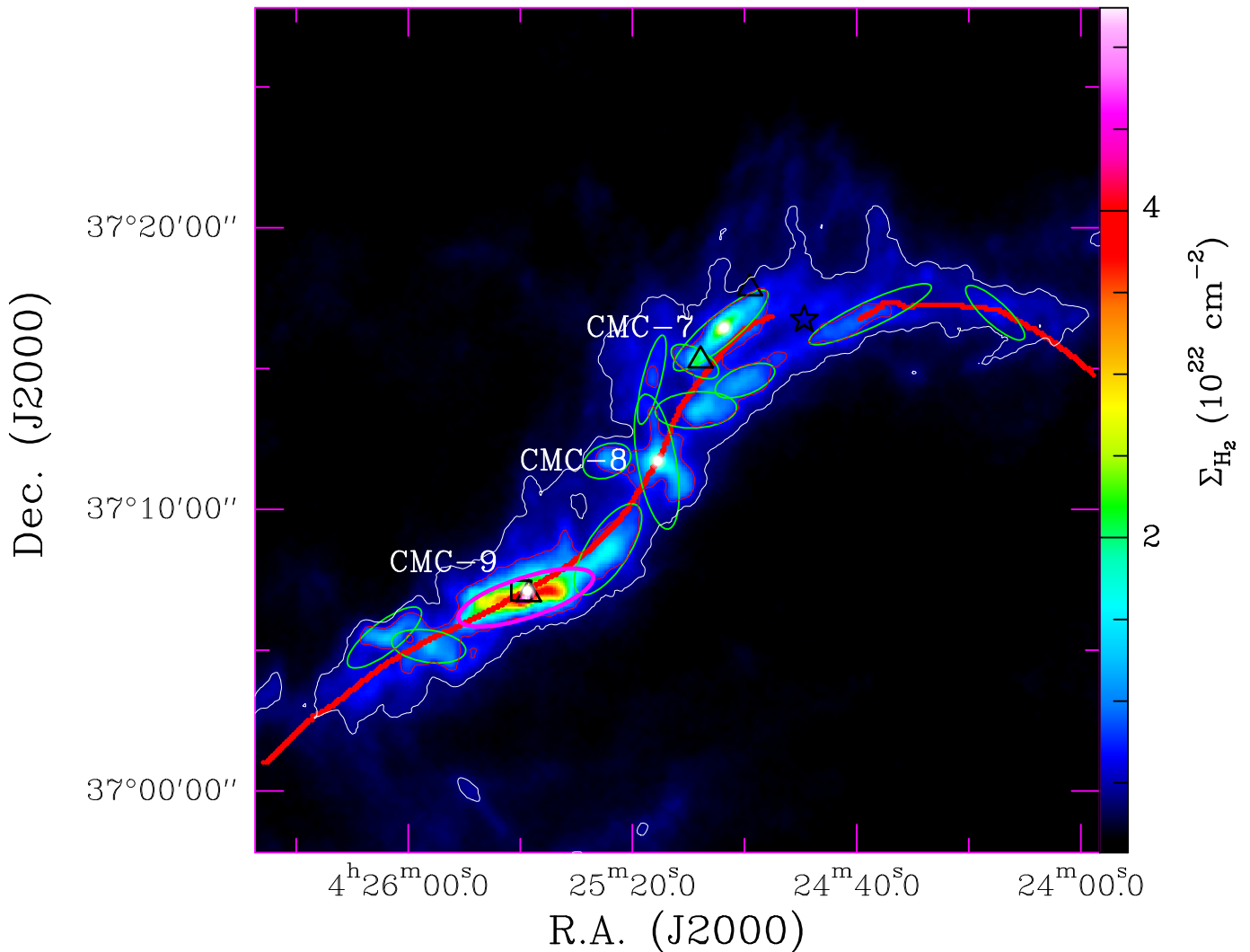


Fig. 12. Filament existing high-mass core. $\sigma = 1.3 \times 10^{21} \text{ cm}^{-2}$ is the noise estimated in the local region from off-sources. The white contour is 3σ . The pink contour is the average surface density threshold for efficient star formation, $116 \text{ M}_\odot \text{ pc}^{-2}$ (Lada et al. 2010), corresponding to $7.3 \times 10^{21} \text{ cm}^{-2}$. The green ellipses are cores. The high-mass cores are plotted with pink ellipses. The white solid circle is the IRAM 30m observation point. The red curve is the skeleton of the filament extracted by getfilaments (Men'shchikov 2013). The black square is a class II YSO. The black triangle is a class 0/I YSO. The five-pointed star is a class III YSO.

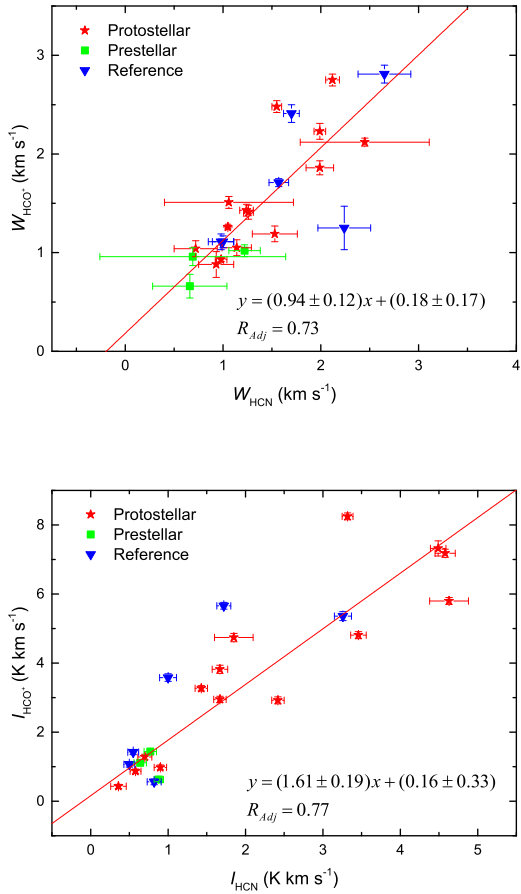


Fig. 13. Line widths and velocity-integrated intensities of HCN and HCO^+ . They follow strong linear relationships, which indicate that HCN and HCO^+ couple well and there are tight chemical connections. The 14 protostellar cores are plotted with red stars, the seven prestellar cores are plotted with green boxes, and the eight observation positions are reference positions that are offset from the cores. They are plotted with blue inverted triangles.